2011-07-07

Eddy Impaction As An Ash Deposition Mechanism: A Theoretical And Experimental Investigation

Minmin Li
Brigham Young University - Provo

Eddy Impaction as An Ash Deposition Mechanism:

A Theoretical and Experimental Investigation

Minmin Li

A thesis submitted to the faculty of
Brigham Young University
in partial fulfillment of the requirements for the degree of

Master of Science

Larry L. Baxter, Advisor
David O. Lignell
Thomas A. Knotts

Department of Chemical Engineering

Brigham Young University

August 2011

ABSTRACT

Eddy Impaction as An Ash Deposition Mechanism:
A Theoretical and Experimental Investigation

Minmin Li
Department of Chemical Engineering
Master of Science

The eddy impaction ash deposition model derived and validated in this document predicts eddy impaction rates as a function of turbulence intensity, boundary layer thickness, and gas velocity. The experimental apparatus introduces small particles (200 nm, 25 μm, and 500 μm diameter) into a gas stream flowing through a horizontal pipe (Re 2,300-8,000). The particles deposit on the pipe wall and the total mass of impacted particles provides a measure of collection efficiency. Experimental results indicate deposition velocity increases with Reynolds number, consistent with eddy impaction theory and based on increased turbulent energy. Eddy impaction also increases with particle size at fixed Reynolds number, again consistent with theory.

Keywords: Eddy Impaction, Ash Deposition, Reynolds Number, Turbulent

ACKNOWLEDGEMENTS

I would like to thank a number of people who have provided me with a great deal of help to complete this project and thesis work. I would like to express my deep appreciation to my advisor, Dr. Larry Baxter, for the opportunity to join this great research group and work on this exciting project. Without his academic and economical supports, this work would never have been completed.

I am grateful to my other committee members, Dr. David Lignell and Dr.Thomas Knotts, for their help and guidance on my research. I am also grateful to Shrinivas Lokare, whose previous work helped me understand this project profoundly. Special thanks to two undergraduate students who work with me, Sayantan Ghosh and Daniel Yeats, for their help on running experiments and setting apparatus, and provide valuable suggestions throughout the process. I am also thankful Cameron Quist for thesis editing and I will thank to Jacob Beutler and David James, it was precious time and fun to discuss and chat with them and it gave me so much help both in academic and daily life.

Thanks also go to all students in BYU combustion group, who offer great research environment thus trigger me inner world to contribute.

Finally, I express my gratitude to my parents and all my friends, their endless love and support are the foundation of my life and the cozy shelter of my sprit.

I would like to thank every hand that helped me directly or indirectly in completion of this project work.

TABLE OF CONTENTS

LIST OF FIGURES

LIST OF TABLES

1 INTRODUCTION

Particle deposition on surfaces fundamentally influences many natural and industrial processes. Issues as diverse as lung disease, ceramic processing, radioactive fallout, dust migration in natural environs, process equipment fouling and erosion, and blood clot formation all fundamentally depend on particle deposition. However, the motivation for this work is energy production through sustainable processes, specifically ash deposition in coal- and biomass-fired combustors and gasifiers.

Coal has been an important energy source for humankind for thousands of years. The earliest reference to the use of coal as fuel is from the geological treatise *on stones* (Lap. 16) by the Greek scientist Theophrastus (c. 371–287 BC). Coal was used in Britain during the Bronze Age (3000–2000 BC), where formed part of the composition of funeral pyres (Britannica 2004; Golas 1999), and as fuel by the 4th century AD in ancient China (Read 1940). Now coal primarily fuels electrical power plants and provides space heating through combustion. World coal consumption was about 6,743,786,000 short tons in 2006 and is expected to increase 48% to 9.98 billion short tons by 2030. China produced 2.38 billion tons in 2006. India produced about 447.3 million tons in 2006. 68.7% of China's electricity comes from coal. The USA consumes about 14% of the world total, using 90% of it for generation of electricity. Generally speaking, approximately 40% of the world electricity production uses coal (EIA statistics).

Coal is the largest source of energy for the generation of electricity worldwide, as well as one of the largest worldwide anthropogenic sources of carbon dioxide emissions. Gross carbon dioxide emissions from coal usage are slightly more than those from petroleum and about double

the amount from natural gas (Joller, Brunner and Obernberger 2007). Along with its energy content, coal combustion produces pollutants such as NO_X, SO_X, CO_2, particulate, Hg, etc. Increasingly stringent EPA emissions regulations increasingly dictate the type of coal and power plant used for power generation. Consequently, the fuel base is changing to reduce pollutants and, in the future, utilization of CO_2-emitting fossil fuels that bear negative effects on global climate. Although the fossil fuels are currently, and will remain for some time, the major resource to meet increasing worldwide energy demands, it is imperative to search for alternate sources of energy. As "renewable" and "clean" being the most desired requirements from alternate fuels, biomass has shown its ability to replace coal in part or in whole in power generation plants.

During recent years, there has been extensive research in combustion of biomass as a single fuel as well as co-fired with coal. Currently, forest and agricultural residues and waste represent the most widely used biomass fuels in energy production. Energy crops represent additional potential biomass resources. In existing pulverized-coal-fired (pc) boilers, biomass co-fired with coal reduces some of emissions from coal (primarily SO_X, NO_X, and CO_2) while increasing the energy conversion efficiency of biomass as compared to dedicated biomass-based systems. Biomass rarely competes effectively with coal in the absence of carbon-emission taxes or credits, but when co-fired with coal it is often the least expensive form of renewable energy generation.

Despite being clean and renewable, biomass has disadvantages such as extensive ash deposition and corrosion problems. Highly variable ash content and chemistry in both coal and biomass result in potential deposition issues in operational facilities. Coal and biomass power plant operation and design depend strongly on ash deposition.

Ash deposition represents a long-standing operational and design research issue. Ash deposition and associated heat transfer represent arguably the single most important parameter influencing boiler size and firing rate. They contribute to corrosion and decrease heat transfer by decreasing effective thermal conductivity and emissivity and increasing effective path length. They also increase weight and stress on components, radically increasing maintenance associated with ash removal. Therefore, ash formation, transformation and deposition models can provide valuable information to help reduce corrosion, fouling and emission problem (Joller et al. 2007). Computer simulations and fuel performance indices help select proper fuels and operating conditions, reducing ash deposition problems. Relatively little quantitative experimental data exist for validating predictions of ash deposition simulations. Detailed and quantitative ash deposition data and models could significantly improve thermal processor (combustor, gasifier, etc.) designs and performance. While many of the mechanisms of ash deposition are well established, such as inertial impaction and condensation, eddy impaction rate expressions and understanding remains largely empirical.

Eddy impaction describes impaction rates associated with particles are too small to transit average fluid boundary layers around surfaces but within the range that they can transit this boundary layer given the extra energy associated with, and the change in boundary layer thickness associated with, turbulent eddy velocity fluctuations. This investigation determines the fundamental mechanisms and theoretical descriptions of eddy impaction, including original model development and experimental investigations. The goal is to provide a sound fundamental basis to replace the existing largely empirical description of this phenomenon.

The dual focuses of this investigation are to present an analytical eddy impaction ash deposition model and experimentally validate this model. This work largely deals with

monodisperse particles in ideal, isothermal flows for which eddy impaction is the only deposition mechanism.

2 LITERATURE REVIEW AND RESEARCH THEORY

This chapter discusses the theory behind important factors related to ash deposition and the research which has been done to characterize deposition-related processes. Coal and biomass combustion are introduced and the various ash properties and deposition mechanisms are described. Different theories from literatures are also discussed in this chapter.

2.1 Background

Coal and other fuels used in power generation boilers vary in ash content and amount. Coal exhibits wide variations in many of its properties, including composition. A full chemical analysis of a sample of a typical coal (see Table 1), called an ultimate analysis, lists the proportions by the main elements that are present, usually carbon, hydrogen, oxygen, nitrogen and sulfur. These analyses are often in terms of dry, ash-free samples, excluding any moisture and inert matter. In such a complex material, theory cannot yet take us from the ultimate analysis to the answers to these questions. A table is shown next containing an example of coal ultimate analysis data and showing significant elements only (Hutagalung 2008). Conversion from one basis to another can be performed using mass balance equations.

A different analysis is needed called proximate analysis, one that reflects the value of the coal to its users. Heating is the essential feature common to all uses of coal, leading either to full combustion or partial-combustion, or the production of other fuels, and it is the sequence from

Table 1 Ultimate analysis of a typical coal

Ultimate Analysis	unit	(AR)	(AD)	(DB)	(DAF)
Carbon (C)	(wt.%)	61.1	61.5	63.2	81.9
Hydrogen (H)	(wt.%)	3	3.02	3.1	4.02
Nitrogen (N)	(wt.%)	1.35	1.36	1.4	1.81
Total Sulfur (S)	(wt.%)	0.4	0.39	0.39	
Oxygen (O)	(wt.%)	8.8	8.8	9.1	

heating to combustion that provides the basis for the most common characterization of different coal types**.** The objective of coal proximate analysis is to determine the amount of fixed carbon (FC), volatile matters (VM), moisture, and ash within a typical coal sample (see Table 2). The variables are measured in weight percent (wt. %) and are calculated in several different bases. AR (as-received) basis is the most widely used basis in industrial applications. AR basis puts all variables into consideration and uses the total weight as the basis of measurement. AD (air-dried) basis neglect the presence of moistures other than inherent moisture while DB (dry-basis) leaves out all moistures, including surface moisture, inherent moisture, and other moistures. DAF (dry, ash free) basis neglect all moisture and ash constituent in coal while DMMF (dry, mineral-matter-free) basis leaves out the presence of moisture and mineral matters in coal, for example: quartz, pyrite, calcite, etc. Mineral matter is not directly measured but may be obtained by one of a number of empirical formula based on the ultimate and proximate analysis. A table is shown next containing an example of proximate analysis data of coal. Conversion from one basis to another can be performed using mass balance equations (Hutagalung 2008).

Table 2 Proximate analysis of a typical coal

Proximate Analysis	unit	(A	(AD)	(DB)	(DAF)
Moisture	(wt.%)	3.3	2.7		
Ash	(wt.%)	22.1	22.2	22.8	
Volatile Matter	(wt.%)	27.3	27.5	28.3	36.6
Fixed Carbon	(wt.%)	47.3	47.6	48.9	63.4
Gross Calorific Value	(wt.%)	24.73	24.88	25.57	33.13

Lignite, subbituminous coal, bituminous coal and anthracite are the major coal ranks in increasing order of heating value or fixed carbon. Coal type, age, elemental composition and other properties generally correlate with rank. The lowest rank coals (lignites) contain high moisture and volatile matter, while the highest rank coals (anthracites) have low volatile and moisture content. Similarly, inorganic material in coals shows variation depending on rank of individual coal. Low-rank coals commonly contain relatively large amounts of organically associated elements such as Na, Mg, Ca, K, and Sr present as salts of organic acid groups, as well as mineral grains, although they commonly contain less chlorine than high-rank coals. By contrast, high-rank coals commonly contain more iron and sulfur than low-rank coals. Variation in such inorganic content changes the deposition and corrosion potential of coals, thus presenting it as one of the most investigated issues in power generation. Figure 1 presents the extent of variation in different coals as well as coals and biomass fuels which are currently among the best renewable energy options for coals. The ultimate analysis for the coals and biomass shown in Figure 1 indicates high carbon content and also lower moisture content (not shown) in coals than biomass. The ash chemistry charts in Figure 2, show that the ash content for coals exhibit modest variation, while that for biomass fuels exhibit large variation. Biomass ash shows higher alkali

and chlorine contents compared to coal ash while coal ash contains sulfur which is undetectable in biomass ash.

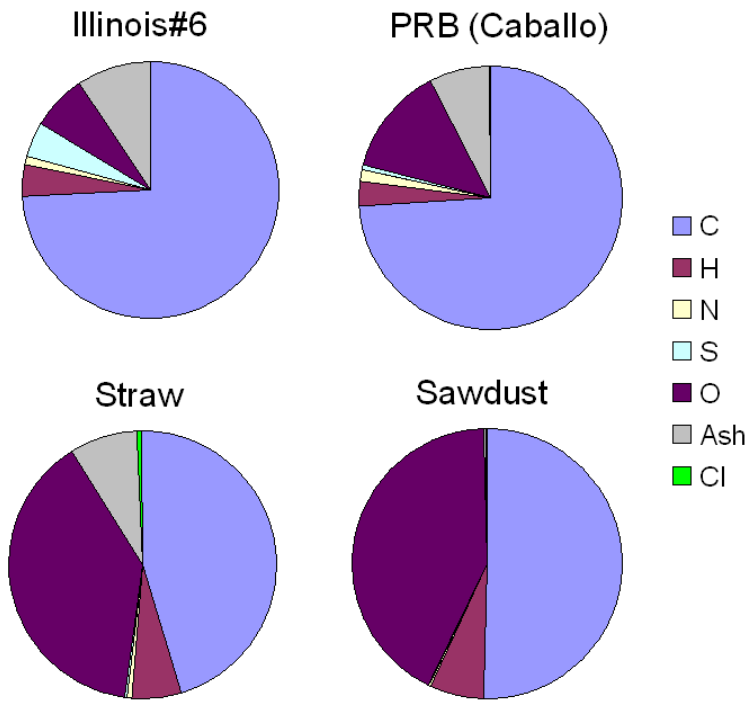

Figure 1 Variation in fuel composition of coals and biomass fuels

Such differences create significant changes in combustion characteristics, making it harder to accommodate a wide variety of fuels in a single furnace as described later in this section.

The pre-combustion factors that affect deposition are inorganic content (amount and composition) within coals and particle size distribution. Inorganic material in pulverized coal exists either as included (i.e. associated with or contained within a carbonaceous coal particle), or "excluded," (i.e. not having any carbonaceous material associated with it). Depending on whether the minerals (e.g. pyrites) are included or excluded, ash formation proceeds differently.

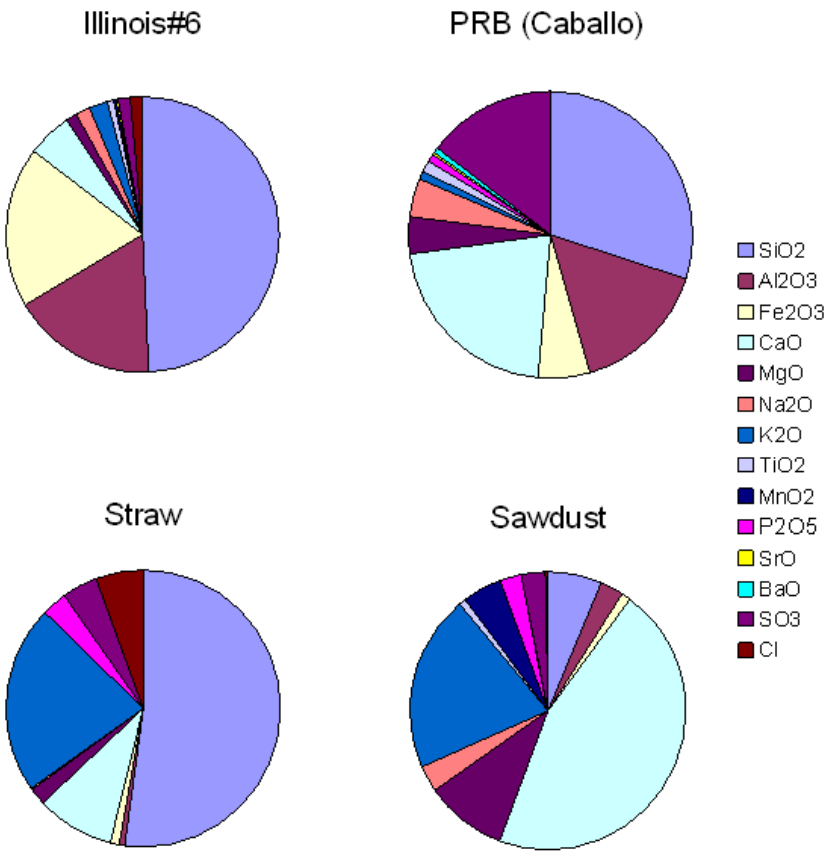

Figure 2 Variation is ash composition of coal and biomass fuels

Srinivasachar and others (Srinivasachar 1990b, Srinivasachar 1990c, Wall 1992) showed that inclusion or exclusion of the minerals affects the surface characteristics of ash particles. For examples, particle stickiness depends on magnetite crystallization time during pyrite transformation. The mineral distribution also determines the ash particles size. Included minerals tend to produce smaller ash particles than excluded minerals. However, excluded minerals fragment more extensively due to inner gas expansion at high temperatures producing smaller ash particles. Following the fragmentation of excluded minerals and/or release of included minerals, these small particles coalesce and produce larger ash particles. Vapor formation from

inorganic species and subsequent recondensation forms the smallest fly ash particles (see following Figure 3).

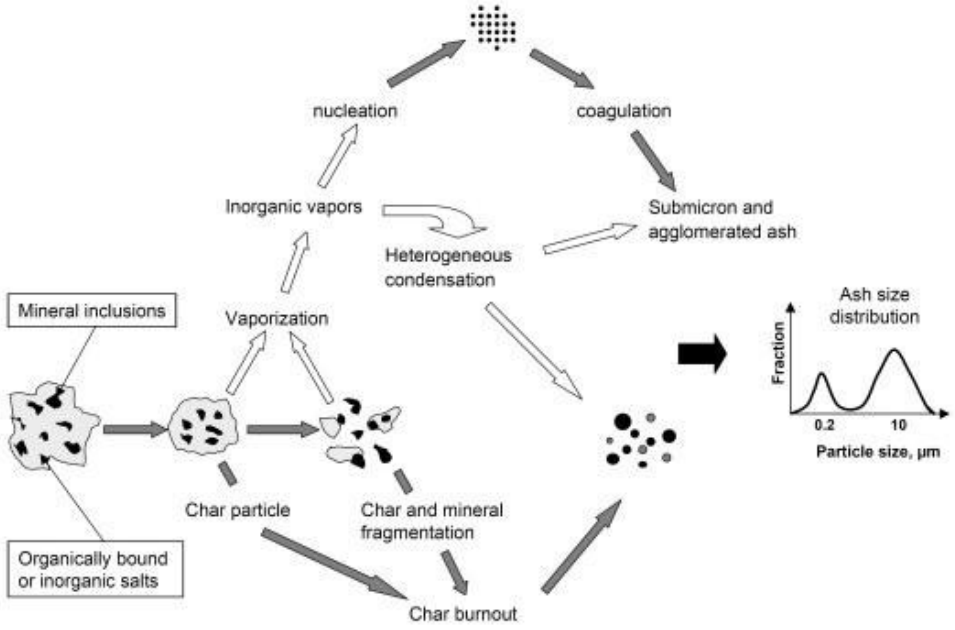

Figure 3 Mineral matter transformation during pulverized coal combustion (Figure taken from www.3me.tudelft.nl)

Post combustion research in deposition mainly involves ash deposit properties such as thermal conductivity, porosity, emissivity, etc. and dependence of these parameters on combustion conditions. As ash deposits grow, their thickness increases and porosity decreases due to sintering, consolidation and slagging, which increase deposit thermal conductivity (Baxter 1998b, Baxter 2000, Robinson 2001a, Robinson 2001b). Many researchers described the connection between the physical structures of a deposit and its radiative properties, qualitatively and mechanistically. The absorptivity and emittance are the most important factors in predicting the thermal behavior of ash deposits in the radiant section of combustors while the thermal conductivity plays a dominant role in the convective and a secondary role in the radiant sections

(Baxter 1988, Baxter 1993, Wall 1993, Wall 1995, Wall T.F. 1996, Baxter 1998a, Baxter 2001, Zbogar et al. 2005).

2.2 Biomass Ash Deposition

An alternative with greater greenhouse gas impact is the displacement of coal with a renewable energy source such as biomass, either as a co-fired fuel in a coal-based system or as a dedicated biomass system. Biomass plays an important role in the production of energy. As an energy source, biomass ranks fourth in the world, providing approximately 12-14 % of the total (domestic and industrial) energy requirement (Green 1994). Biomass combustion is more significant (~35 %) in developing countries (Green 1994), (Hein and Bemtgen 1998), (Jenkins 1998a). Biomass residues represent the most readily accessible and often least costly form of biomass available today. These include residues from the forest product industries, agricultural residues, and non-recyclable consumer products such as paper. A second category of biofuels includes energy crops, which come in both woody (hybrid poplar, willow, etc.) and herbaceous (switchgrass, miscanthus, etc.) varieties of biomass (Jenkins 1998a).

Other hydrocarbon fuels such as coal, gasoline, and heavy hydrocarbons produce large amount of CO_2 that accumulate in the atmosphere during combustion. In contrast, biomass fuels come from plants, which consume CO_2 during growth. The CO_2 is then liberated when the fuel is burned. Biomass combustion is therefore nominally CO_2 neutral, but assuming some fossil fuel is consumed for fuel cultivation, transportation, and preparation, some net CO_2 is produced. Thus, biomass can be shown to reach a 95% CO_2 closure when burned alone (Yuanyuan Shao 2010). These results in a net greenhouse gas impact that is near zero and under some conditions can be less than zero (by avoiding emissions of more potent greenhouse gases such as methane during

decay or other slow biological processes). A study by Mann and Spath (Mann 1999), indicates that co-firing biomass with coal decreases CO_2 emissions by 5%-15% and thus, it creates a potential solution for greenhouse gas reduction. In addition to the renewable, sustainable, indigenous advantages of biomass, its use often decreases or eliminates waste streams that otherwise fill landfills or decay on surfaces (Hein and Bemtgen 1998, Jenkins 1998a). Thus biomass fuels represent one of the best solutions for both increased energy and reduced net CO_2 production. Along with cofiring, the opportunities for increasing biomass energy production exist in dedicated facilities as well, which are the boiler facilities where biomass is the only fuel used in combustion for power generation.

Unfortunately, the use of biomass in many combustion systems can produce added operating difficulties particularly related to ash deposition and corrosion. Many biomass fuels exhibit such unattractive behaviors. They commonly decrease boiler efficiency due to high moisture contents or cold-air injection systems.

Although potassium occurs in minor concentrations in biomass fuel compared to silica, its level of concentration is 4-5 times that found in coal and generally high compared to most fuels. Similarly, chlorine content of biomass is higher than that of coal, which leads to some biomass fuels producing high concentrations of alkali chloride in combustion gas. These gas-phase alkali chlorides form a smooth and sticky condensed layer on superheater tubes enhancing ash deposition processes (Kaufmann 2000, Lokare 2003, Coda 2001, Baxter 1998b, Bakker 2002). Agricultural waste products, such as straws, can have large ash fractions, with alkali chlorine and silica as the major constituents. These alkali salts also play a significant role in deposition due to their ability to bind ash particles together through sintering or chemical reactions. These higher degrees of ash deposition are sometimes associated with corrosion.

Alkali, chlorine and silicates are the main fractions of the ash deposit irrespective of the fuel type. The differences in absolute amounts of these compounds are due to the elemental fuel composition and the combustion properties. Thermodynamically, alkali chlorides are the most stable form of alkali and chlorine in the gas phase at flame temperatures (Wall 1995, Jenkins 1998b). When chlorine presence in the fuel is negligible, corrosion can still proceed by the formation of sulfates in large amounts at high surface temperatures. In particular, alkali trisulfates are known to be aggressive on heat transfer surfaces (Robinson 1998).

2.3 Ash Analysis and Deposit Characteristics

An analysis of coal ash may also be carried out to determine not only the composition of coal ash, but also to determine the levels at which trace elements occur in ash. These data are useful for environmental impact modeling, and may be obtained by spectroscopic methods such as ICP-OES or AAS. An example of coal ash composition is shown on the following (Table 3).

Ash deposition characteristics are known to be influenced by coal types (ash constituents, melting temperature, distribution of mineral matter, etc.), reaction atmosphere, particle temperature, surface temperature of a heat exchanger, material of its surface, flow dynamics and so forth. A number of reviews relating to ash deposition characteristics have been already reported. For instance, the advanced analytical method of ash constituents in coal by a Computer Controlled Scanning Electron Microscopy (CCSEM) is useful for the discussion on chemical aspect of the ash deposition (Zygarlicke and Steadman 1990). Srinivasachar (Srinivasachar 1990a) and Vuthaluru (Vuthaluru 2004) have studied formation of the ash intermediates, which consist of gases, liquids and solids. Raask (Raask 1984) elucidated deposit initiation, and Walsh (Walsh 1990) and Baxter (1998) studied deposit characteristics and growth. Beer (Beer 1992)

Table 3 A typical coal ash composition

Oxides	wt.% of ash (Calculated)	Elements	wt.% of ash (Measured)
Na_2O	0.35	Na	0.26
MgO	0.48	Mg	0.29
Al_2O_3	20	Al	10.6
SiO	74.1	Si	34.6
P_2O_5	0.05	P	0.05
K_2O	1.1	K	0.92
CaO	0.68	Ca	0.49
TiO_2	0.8	Ti	0.48
Mn_3O_4	0.06	Mn	0.05
Fe_2O_3	3.25	Fe	2.28

tried to develop modeling ash behaviors. Benson (Benson 1993) summarized the behavior of ash formation and deposition in coal combustion. Even from those references, however, precise and quantitative knowledge on the ash deposition phenomena during coal combustion or gasification at high temperature is insufficient since the deposition strongly depends on coal types. Consequently, it is desirable to study key parameters occupying ash deposition characteristics even though coal type is varied.

Beside composition of coal ash, ash fusion point is also one significant parameter in ash analysis. The optimum operating temperature of coal processing will depend on the gas temperature and also the ash fusion point. Melting of the ashes may cause them to stick to the walls of the reactor and result in a build-up.

One of the primary problems associated with the use of coal in utility boilers is the deposition of inorganic constituents on the heat transfer surfaces (slagging and fouling). Ash deposition leads to reduced heat transfer in the boiler and corrosion of boiler tubes, which may

result in reduced generating capacity and unscheduled outages. Although soot blowing and wall blowing are routinely used to manage deposition, unexpected or uncontrolled deposition can still occur at locations inaccessible to the cleaning devices, or at locations where the bonding strength between the wall and the deposit is too strong for cleaning equipment to be effective. Deposition problems are frequently associated with a change in fuel characteristics and/or boiler operating conditions.

2.4 Ash Deposition Properties

Power generation systems utilize thermal energy produced during combustion to generate electricity. This process operates a maximum efficiency when there are no deposits on the superheater tubes. However, in reality, it is impossible to keep the superheater tubes free from deposits. Thus, ash deposits act as an extra thermal resistance to the energy transfer process, lowering the efficiency. In combustion systems, the thermal energy transfer from flame gases to exterior surfaces of ash deposits is by radiative and convective heat transfer. Heat transfer through the ash deposit and superheater tube is by conduction, and then by convection to the inside fluid stream. Taking this major drawback into account, it is very important to know the physical properties of ash deposits. For conduction, thermal conductivity and ash deposit thickness are key variables affecting heat transfer. For radiation, the absorbtivity and emittance are important (Hein and Bemtgen 1998). Deposit strength, the ability of ash deposit to resist forces induced by the fluid dynamics and gravity, is critical in determining whether particles remain on the surface or are easily removed by fluid shear forces. These properties effect boiler operation and the surface temperature of the deposit, but have little effect on the deposition

characteristics of the particles. The particle size, melting temperature, and stickiness or sintering propensity are the important properties contributing to the deposition rate.

2.4.1 Morphology and Strength

Strength relates to a property of the bulk deposit, not a single particle and represents the deposits ability to resist stress without plastic or catastrophic deformation. Deposit strength development relates to the physical microstructure of the deposit. As individual particles in the deposit increase, contacting efficiency with neighboring particles and strength increases significantly. Contacting efficiency increases as particles sinter, as vapor condenses or liquids accumulate around particles, and as deposits consolidate (Baxter 1998). The cohesive forces that cause these ash particles to stick together are of varying types such as, van der Waals, surface tension, electrostatic, crystallization at contact points, and interlocking of particles. Deposit strength development is important to study because in order for low temperature deposits to block the flow through a system or cause damage to system components, they must develop more strength than is necessary to hold the ash in place against gravity. Comparing the ash deposition rate with strength development rate (shedding index) before applying any means to remove deposits is an area of research interest (Hurley 1996).

2.4.2 Emissivity and Absorbtivity of Deposits

Most ash deposits show spectral variation in their emissivity. The spectral dependence is due in part to a wide range of mineral content in the deposits and in part to deposit morphology. This variation gives rise to a temperature-dependent total or effective emissivity.

During radiative heat transfer, particles generally are less gray with particle size, rank of the fuel and extent of devolatilization decrease. The spectral and total emittances generally

increase with increasing rank of fuel and particle size. As the extent of devolatilization increases, the particle emittance can increase, decrease or remain constant, depending on the region of the spectrum being considered (Baxter 1988).

2.4.3 Thermal Conductivity

The thermal conductivity of ash deposits represents the second major variable controlling heat transfer rates in boilers. The potentially complex chemical species formed in ash deposits do not all have conductivities with well-known dependencies on temperature (Baxter 1996). Current theory is that conductivities depend strongly on the deposits physical microstructure and porosity (Baxter 2000, Robinson 2001). Heat transfer through porous media can more than an order of magnitude less efficient through many boiler deposits than it would be through non-porous samples of the same composition. Thermal conductivity has been observed to increase with increasing particle size and, in the case of fine, non-sintered dusts, to approach the value of air (Boow 1969).

2.4.4 Ash Viscosity

Slagging combustors offer the potential advantages of producing more environmental friendly ash than dry-walled combustors and of increased ash capture and remove in the early stages of the combustion process. Some combustion contractors recognize these advantages and are considering slagging combustors as part of their proposed systems. In a slagging combustor, ash viscosity plays the role of the dominant design consideration after the same manner as deposit strength, tenacity and thermal shock resistance do in dry-walled systems. Correlations of deposition viscosity have been proposed by several investigators (Kalmanoitch 1988, Srinivasachar 1990a) based in large measure on the early work by Urbain (Urbain 1981). These

models are based on relationships and theory from the glass-making industry and represent correlations of viscosity with elemental composition.

2.4.5 Deposit Porosity

Deposit porosity plays a critical role in determining most of the physical and heat transfer properties of the deposit. The development of deposit porosity is influenced by ratio of particle to condensate in the deposit, the sintering of granules in the deposit, and the generation of gases in fluid materials (Raask 1984, Jagota, Dawson and Jenkins 1988, Jagota 1990).

2.4.6 Rate of Accumulation

Steady-state ash deposition process may still have transient effects. This is because, as a deposit layer builds to greater thickness, the rate of heat conduction continues to decrease. Thus, during the development of a deposit layer, the temperature gradient through the deposit and therefore the temperature of the deposit surface will continuously increase, resulting in sintering and fusion of deposit particles (Wall 1995)

It has been shown that the radiative and conductive properties of ash deposits in coal-fired furnaces depend on the physical and chemical character of the deposit. This character changes as deposits form, grow and mature due to the retention of different elements in various proportion over time and due to increasing homogeneity of deposits because of sintering and melting.

2.5 Ash Deposition Mechanisms

At least five physical processes control ash deposition rates: inertial impaction, eddy impaction, thermophoresis, condensation, and chemical reaction (Baxter 2000). A deposition rate

based on these mechanisms is described by Equation 1.

$$\frac{dm}{dt} = I \times G + E + T + C + R \quad (1)$$

Where:

$\frac{dm}{dt}$= Deposition rate

I = Inertial impaction rate

G = Capture efficiency

E = Eddy impaction rate

T = Thermophoretic deposition rate

C = Condensation rate

R = Chemical reaction rate

2.5.1 Inertial Impaction

Particles deposited on a surface by inertial impaction have enough inertia to traverse the gas stream lines and impact the surface. With increasing diameter, the inertia of the particles grows and makes the particles stray more easily from the gas stream line. Inertial impaction frequently dominates the other deposition mechanisms in terms of mass accumulation [3-5]. The particle capture efficiency (G) describes the propensity of particles to stay on the surface once they have impacted it. Inertial impaction occurs when the momentum of the particle toward a surface is large enough to overcome drag forces produced by fluid flow, which direct particles around the tube. As a result, particles pass through the boundary layer and impact the surface. Both particle and surface properties, such as the roughness of a metal surface and ability of the

particle or surface to deform and absorb energy, play significant effect on determining the particle capture efficiency.

The measure for inertial impaction includes two parameters: (1) impaction efficiency (η), which governs particle impaction and is defined as the ratio of the number of particles impacting a target to the total number of particles flowing through a projected target area; (2) capture efficiency, which determines the particle capture extent and is defined as the ratio of the number of particles captured by the target surface to the total number of particles that have impacted the target surface. Impaction efficiency is a function of the generalized Stokes number and particle Reynolds number. Rosner (Rosner 1986) recommended an expression for impaction efficiency as a function of the generalized Stokes number of the following type:

$$\left(Stk_{eff}\right) = 1 + b\left(Stk_{eff} - a\right) - c(Stk_{eff} - a)^2 + d(Stk_{eff} - a)^3 \quad (2)$$

where a = 0.125, b = 1.25, c = -0.014, d = 0.0000508

$$Stk_{eff} = \frac{\rho_p d_p^2 v_p}{9\mu_g d_c}\psi \quad (3)$$

Here, subscripts 'p', 'g', and 'c' stand for particle, gas, and cylinder, respectively, while ρ, μ, d and V indicate density, viscosity, diameter, and velocity, respectively. Ψ is the non-Stokes drag correction factor. Lokare (Lokare 2008) demonstrated that the original Rosner coefficients, based on predicted particle trajectories in potential flow fields around targets, predict impaction efficiencies uniformly too high and in error by as much as 30%. Alternative sets of coefficients for the same geometries based on more sophisticated modeling and confirmed by experiment are for inviscid flow a=0.1238, b=0.134, c=-0.034, d=0.0289 and for viscous flow a=0.1101, b=2.0762, c=-0.2553, d=-0.0224 (see Figure 4).

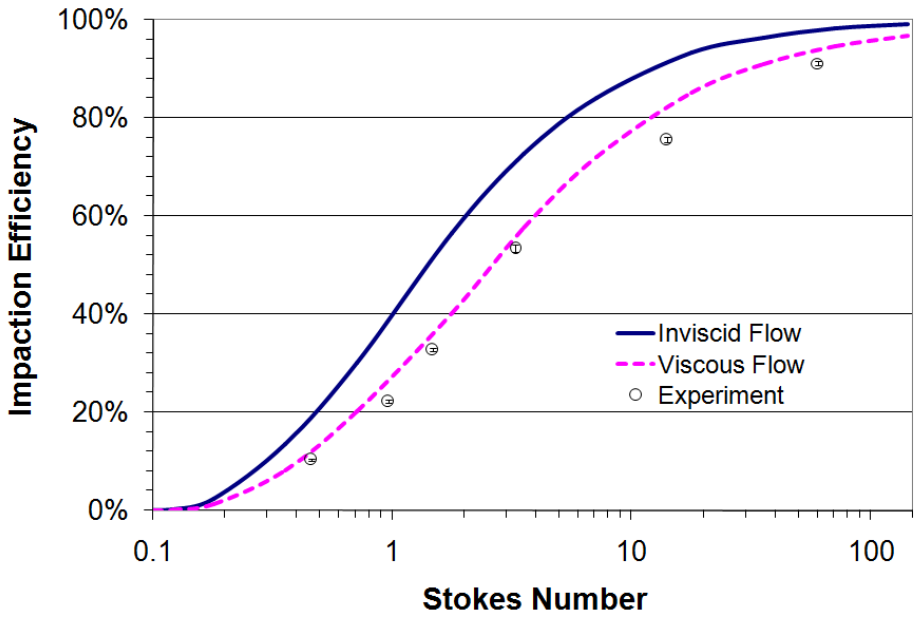

Figure 4 Impaction efficiency variation with Stokes number

2.5.2 Eddy Impaction

Eddy impaction (E) is a process by which small or light particles gain inertia from eddies to impact the surface. It involves fine ash particles that have been entrained in turbulent eddies. These eddies add momentum to the particles and change boundary layer thickness such that particles have enough momentum to impact tube surfaces even though they would be too small to make an impact based on average gas velocities. Most formulas are empirical expressions that are based on conditions far removed from boilers. It will detail discussed later.

2.5.3 Thermophoresis

Thermophoresis (T) is the process of particle motion in a gas due to local temperature gradients. Thermophoresis is important when particle size is small and temperature gradients are large. Particles drift toward a cold surface, or down the temperature gradient, under the influence

of thermophoresis (Postelnicu 2007). Thermophoretic deposits have a finer grain (sub-micron particles) and are more evenly distributed around a tube surface than deposits that are formed by inertial impaction. As the ash accumulates on the surface of the tube, the temperature gradient between the flue gas and tube surface decreases, and the thermophoresis deposition decreases and finally disappears (Postelnicu 2007).

2.5.4 Condensation

Condensation (C) is the mechanism by which vapors (mainly alkali chlorides or hydroxides) collect on cooled surfaces. If the partial pressure of a vapor at a relatively cold surface temperature exceeds the vapor pressure, the vapor condenses on the tube. Possible mechanisms for condensation include: (1) condensation on thermophoretically deposited fume material from the bulk gas phase in the boundary layer; (2) condensation of vapors within the thermal boundary layer and subsequent thermophoretic deposition of these particles or (3) heterogeneous condensation of vapors on the heat transfer surface. Condensates are common in fuels such as biomass and low-grade coal, which contain greater percentages of inorganic materials in vaporizable form compared to other fuels. Condensation is more rapid on the leading edge of surface than at the trailing edge due to of the relative magnitudes of heat and mass transfer coefficients.

2.5.5 Chemical Reaction

Heterogeneous chemical reactions (R) between the gas and either the existing deposited materials or the surface of the tube can also change the total ash deposits. The rate of conversion depends on mass transfer rates to the surface and on chemical kinetics of the heterogeneous reactions involved. The most important chemical reactions with respect to ash depositions

include: (1) sulfation, (2) alkali absorption, and (3) oxidation. Compounds containing alkali or alkaline earth metals such as sodium, potassium, and calcium are the principle sulfating species. These elements readily form hydroxides or chlorides at flame temperatures that sulfate at the cooler surface temperatures. Silica absorbs alkali material to form silicates as an additional example of chemical reaction. Silicates are less rigid and melt at lower temperatures than silica (SiO_2). The transformations of silica to silicates in deposits can induce sintering and significant changes in deposition properties. Finally, residual carbon and some inorganic species such as iron sulfides oxidize on the surface.

2.5.6 Other Mechanisms

There are several other mechanisms of deposit growth. Among these are electrostatic interactions, photophoresis, and Brownian motion. However, compared with inertial impaction, eddy impaction, thermophoresis, condensation, and chemical reaction, they play a minor role in ash deposition.

Boiler design and operation, especially combustion chamber aerodynamics, affect deposition in the boiler. Highly swirling flows may throw particles to the heat transfer surfaces, resulting in enhanced deposition (Baxter 2000). According to Lee (Lee 1999), the amount of fly ash trapped in the boundary layer and the particle arrival rate are very sensitive to particle size and density. Critical deposition properties, such as thermal conductivity and strength, depend heavily on the deposit microstructure (Zbogar 2006). The measurements by Kweon (Kweon, Ramer and Robinson 2003) indicated that high-temperature deposits have more interconnected and coarser structures than low-temperature deposits.

3 OBJECTIVES

The objectives of this research are to collect mass deposition data and develop models that predict eddy impaction deposition rates and mechanisms. This investigation will extend the existing free-flight models for fine particles. Fundamental experimental work applicable to combustion, gasification, oxyfuel firing, and other reaction conditions motivates most of this work. Since it is not possible to isolate eddy impaction rates from other rates in practical flows, this work will largely deal with monodisperse particles in ideal, isothermal flows for which eddy impaction is the only plausible deposition mechanism. The remainder of this document presents first the model development, followed by the experimental results and discussion.

4 MODEL BUILDING AND EXPERIMENT SET UP

4.1 Model Description

Beginning with a force balance on a particle, where the primary forces are drag, weight, and buoyancy

$$\sum \vec{F} = \frac{d\, m_p \vec{v}_p}{dt} = \vec{F}_D + \vec{F}_g \tag{4}$$

For small particles (small Reynolds numbers), the drag coefficient C_D for sphere is,

$$C_D = \frac{24}{Re} = \frac{24\mu_g}{\rho_g d_p |\vec{u}_g - \vec{u}_p|} \tag{5}$$

Leading to

$$\frac{d\,\vec{u}_p}{dt} = \beta(\vec{u}_g - \vec{u}_p) + \vec{g} \tag{6}$$

where $\beta = \frac{18\mu_g}{\rho_p d_p^2\, C_C}$

and C_C is the Cunningham correction factor, which modifies the drag law for particles that are comparable to or smaller than gaseous mean free paths and hence cannot be treated as if in a gas continuum. The Cunningham correction factor defines as,

$$C_c = 1 + \frac{2\lambda}{d}\left[A_1 + A_2 \exp\left(-\frac{A_3 d}{\lambda}\right)\right] \tag{7}$$

where A_1, A_2, and A_3 = 1.257, 0.4, 0.55 in air, respectively.

The first objective is to estimate the relative magnitude of particle velocity fluctuations relative to those of turbulent, entraining gas. If we assume a gas has a periodic, possibly decaying turbulence/fluctuating character such that the gas velocity is given by

$$u_g = A\ \exp(-rt)\sin(b+st) \tag{8}$$

where r, b, and s are arbitrary generally positive constants with r and s representing inverse time constants associated with the decay and the fluctuations, respectively, and b being a dimensionless phase shift, and A is an arbitrary peak fluctuation magnitude. As formally derived later, the differential equation describing the response of particle velocity to the gas velocity is

$$\frac{du_p}{dt} = \beta\left(u_g - u_p\right) + g = \beta\left[A\ \exp(-rt)\sin(b+st) - u_p\right] + g \tag{9}$$

The solution to this equation with an initial condition of $u_p(t=0) = up0$ is

$$\begin{aligned} u_p = \frac{e^{-t\beta}}{[s^2+(r-\beta)^2]\beta}\Big(&[s^2+(r-\beta)^2]\left[\left(e^{t\beta}-1\right)g + u_p^0\beta\right] \\ &+ A\beta^2\big\{s\cos b + (r-\beta)\sin b \\ &- e^{t(\beta-r)}[s\cos(b+st) + (r-\beta)\sin(b+st)]\big\}\Big) \end{aligned} \tag{10}$$

Ignoring the impacts of gravity renders,

$$\begin{aligned} u_p = \frac{e^{-t\beta}}{[s^2+(r-\beta)^2]\beta}\Big(&u_p^0\beta[s^2+(r-\beta)^2] \\ &+ A\beta^2\big\{s\cos b + (b-\beta)\sin b \\ &- e^{t(\beta-r)}[s\cos(b+st) + (r-\beta)\sin(b+st)]\big\}\Big) \end{aligned} \tag{11}$$

The parameter a is only a phase shift in the fluctuating component. If we assume that all phases are equally likely, the average of the square of the particle velocity with respect to the phase shift is

$$\overline{u_p^2} = \frac{\int_0^{2\pi} u_p^2 da}{\int_0^{2\pi} da} = \frac{\int_0^{2\pi} u_p^2 da}{2\pi} \tag{12}$$

or

$$\overline{u_p^2} = \frac{e^{-2t\beta}}{s^2 + (r-\beta)^2}\left({u_p^0}^2 [s^2 + (r-\beta)^2] + \frac{(A\beta)^2}{2}\left\{1 + e^{t(\beta-r)}\left[e^{t(\beta-r)} - 2\cos(st)\right]\right\}\right) \tag{13}$$

Similarly,

$$u_g^2 = \frac{\int_0^{2\pi} u_g^2 da}{\int_0^{2\pi} da} = \frac{\int_0^{2\pi} u_g^2 da}{2\pi} = \frac{A^2}{2} e^{-2rt} \tag{14}$$

So

$$\frac{\overline{u_p^2}}{\overline{u_g^2}} = \frac{2e^{2t(r-\beta)}}{A^2[s^2 + (r-\beta)^2]}\left({u_p^0}^2 [s^2 + (r-\beta)^2] + \frac{(A\beta)^2}{2}\left\{1 + e^{t(\beta-r)}\left[e^{t(\beta-r)} - 2\cos(st)\right]\right\}\right) \tag{15}$$

This expression includes the effects of initial particle velocities and phase differences. Usually, interest in the particle behavior long after the initial release. If the particle responds rapidly compared to the rate of turbulence decay, that is, if $r < \beta$, the limit of this expression at

long times is

$$\lim_{t\to\infty, b<\beta} \frac{\overline{u_p^2}}{\overline{u_g^2}} = \frac{\beta^2}{s^2 + (\beta - r)^2} \tag{16}$$

This expression is valid for all flows in with homogeneous ($r = 0$) or nearly homogeneous turbulence and for all flows where the turbulence decay rate is slow compared to the particle response time. The expression shows that the ratio of the square of the particle velocity fluctuation to that of the gas increases as the particles become smaller or less dense (β increases), decreases as the gas fluctuation frequency becomes larger (s become larger), and can only be greater than unity when the turbulence decay rate is a measureable fraction of the particle response rate. All of these trends align well with intuition. That is large and dense particles follow the gas fluctuations less precisely as small ones; no particles follow extremely rapid fluctuations; and particle velocity fluctuations cannot exceed those of the gas that drives them unless the gas fluctuation rate is rapidly decreasing. If the gas turbulence is decaying more rapidly than the particle response time, the more complicated expression involving the initial particle velocities is required for the analysis.

Considering only the velocity component normal to a surface (dropping the vector notation), assuming drag forces are much more significant than gravity ($\vec{g}/\beta \to 0$)

$$u_p = u_g + \left(u_p^0 - u_g\right)\exp(-\beta t) \tag{17}$$

where only one velocity component is considered.

The solution to the Equation 6 is

$$\frac{u_p}{u_\mathrm{p}^0} = \exp(-\beta t) \tag{18}$$

indicating that particle position varies in time according to the integral of the velocity with time, namely

$$x_p = \frac{u_{\mathrm{p}}^0[1-\exp(-\beta t)] + x_p^0\,\beta}{\beta} \tag{19}$$

The maximum distance the particle travels depends linearly on its initial velocity and inversely on β, as follows

$$\lim_{t\to\infty} x_p = \frac{u_{\mathrm{p}}^0 + x_p^0\,\beta}{\beta} \equiv x_p^\infty \tag{20}$$

where u_{p}^0 is the initial velocity, which we will treat as a statistically varying function with a mean of zero and a standard deviation of the root-mean-square value of the fluctuation, u'_p. Assuming the initial position is at the edge of the boundary layer, δ is the boundary layer thickness and is taken as zero (which is an arbitrary value, so this does not decrease the general application of this approach), fluctuations sufficient to deposit a particle on the surface are

$$u'_p > \beta\delta \tag{21}$$

as previously shown, if the particle is in the Stokes regime ($C_D = 24/Re$)

$$\beta = \frac{3\pi d_p \mu_g}{m_p C_C} = \frac{18\mu_g}{C_c \rho_p d_p^2} \tag{22}$$

The magnitudes of particle and gas velocity fluctuations are related by

$$\frac{u'^2_{p,rms}}{u'^2_{g,rms}} = \frac{\beta^2}{(\beta+r)^2 + s^2} \tag{23}$$

where *s* is the gas fluctuation characteristic frequency and *r* is the gas turbulence decay rate in the sense that the gas velocity field has an approximate temporal characteristics of

$$u'_g = \mathrm{A}\sin(st)\exp(rt) \tag{24}$$

where *r* is negative if the gas fluctuations are decaying.

The ratio is between root-mean-square fluctuations. This relationship shows how very small particles (large β) exhibit similar fluctuations as the gas, whereas the fluctuations of large particles are damped compared to those of the gas unless the turbulent flow field is in rapid decay. In that case the large particle fluctuation may actually exceed that of the gas. Very rapid gas fluctuations (large s) induce minor particle velocity fluctuations whereas slow gas fluctuations in a homogeneous (non-decaying) turbulent flow lead to particle fluctuations of the magnitude as the gas. This leads to the relationship

$$u'_{g,rms} = \frac{\sqrt{(\beta + r)^2 + s^2}}{\beta} u'_{p,rms} \tag{25}$$

Assuming a Gaussian distribution of gas velocity fluctuations, that is, that the probability density function for the gas fluctuations is given by

$$g(u_g) = N(0, u'_g) = \frac{1}{\sqrt{2\pi} u'_g} \exp\left[-\frac{u_g^2}{2u'^2_{g,rms}}\right] \tag{26}$$

then the particle density function for particle fluctuations is

$$\begin{aligned} h(u_p) &= N\left(0,\ u'_p(u'_g)\right) \\ &= \frac{\beta}{\sqrt{2\pi[(\beta + r)^2 + s^2]} u'_{p,rms}} \exp\left[-\frac{(\beta u_p)^2}{2[(\beta + r)^2 + s^2] u'^2_{p,rms}}\right] \end{aligned} \tag{27}$$

The fraction of particles depositing on the surface is the same as the probability of x_p^∞ exceeding the boundary layer thickness δ, and is given by

$$\eta = p(x_p^\infty > \delta) = \frac{1}{2}\mathrm{erfc}\left[\frac{\beta^2 \delta}{u'_{p,rms}\sqrt{2[(\beta + r)^2 + s^2]}}\right] = \frac{1}{2}\mathrm{erfc}\left(\frac{\beta\delta}{u'_{g,rms}\sqrt{2}}\right) \tag{28}$$

Defining an eddy impaction Stokes number as the inverse of the argument of the complementary error function above.

The eddy impaction Stokes number is

$$St' = \frac{u'_{g,rms}\sqrt{2}}{\beta\delta} = \frac{u'_{p,rms}\sqrt{2[(\beta+r)^2+s^2]}}{\beta^2\delta} \tag{29}$$

This Stokes number increases with increasing turbulent intensity and yields capture efficiency as indicated below (see Figure 5). Figure 5 is a plot of eddy impaction efficiency vs. this dimensionless Stokes number $\frac{u'_{p,rms}\sqrt{2[(\beta+r)^2+s^2]}}{\beta^2\delta}$, or equivalently, $\frac{u'_{g,rms}\sqrt{2}}{\beta\delta}$, up to a value of 3.0. The impaction efficiency approach at a value of 0.5. The eddy impaction efficiency increases with increasing particle/gas turbulent intensity and decreases with increasing boundary layer thickness. This trend agrees with intuition. Perhaps less intuitively, eddy impaction efficiency increases with increasing particle size for a given gas velocity fluctuating environment.

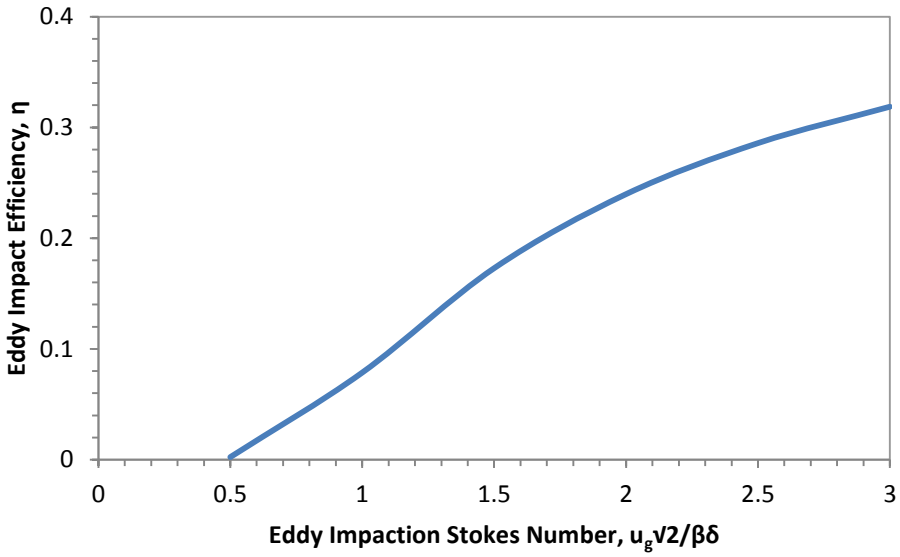

Figure 5 Plot of eddy impaction efficiency vs. the dimensionless parameter

Since turbulent boundary layers are exceedingly thin and the laminar sublayer represent a small fraction of the total boundary layer, particle sizes often compare to or greatly exceed the

laminar sublayer thickness in this analysis. Under such conditions, the effectively thickness of the laminar layer would be expected to increase with increasing particle size for the same fundamental reasons and possibly in a quantitatively similar manner as turbulent drag coefficients increase with increasing surface roughness. These well-established trends do not lend themselves to fundamental analysis but are well known factors in empirical correlations of, for example, a pipe friction factor. In this investigation, we anticipate that the ratio of particle size to laminar sublayer should represent an additional important, albeit probably empirical, parameter describing deposition rates. A candidate correlating expression for the deposition velocity is, therefore,

$$u_{p,dep} = \frac{u_p'}{2}\,\mathrm{erfc}\left(\frac{1}{St'}\right) = \frac{u_g'}{2}\frac{\beta}{\sqrt{(\beta+r)^2+s^2}}\left(\frac{d_p}{\delta}\right)^n \mathrm{erfc}\left(\frac{1}{St'}\right) \tag{30}$$

where n is empirically determined. There may be more accurate expressions that can be derived based on well-established dependence of the friction factor on surface roughness.

For boundary layer thickness, according to Frank (Frank 2005),

$$\frac{\delta}{d} = \frac{14.1}{\mathrm{Re}\,\mathrm{f}^{1/2}} \tag{31}$$

Where d is diameter of the pipe, f is friction factor and can be calculated as follows:

$$\frac{1}{\mathrm{f}^{1/2}} = -1.8\log\frac{6.9}{\mathrm{Re}} \tag{32}$$

Toonder and Nieuwstadt (Toonder and Nieuwstadt 1997) performed Laser Doppler Velocimety (LDV) profile measurements of a turbulent pipe flow of water at different Reynolds number. The conclusions of these measurements are summarized in Figure 6. f^+ represents the dimensionless frequency and $\Psi u_r u_r$ is defined proportional to the mean square of the fluctuating signal. There is a clear Reynolds-number dependence for the mean velocity profile non-

dimensionalized with wall variables in the logarithmic region for Re< 25000. It shows the turbulence intensity, increases with increasing Re, and its peak positions shifts away from the wall.

To prove the relationship between the frequency and Reynolds number, use ln(f+) = -2 to calculate the turbulent frequency in my system. According to Toonder and Nieuwstadt (Toonder and Nieuwstadt 1997),

$$f^{+}_{frequency} = \frac{f_{frequency}\nu}{{u_*}^2} \tag{33}$$

here *v* is the kinematic viscosity of gas, u_* is friction velocity,

$$u_* = (f/2)^{1/2}\bar{u} \tag{34}$$

where $\bar{u}$ is the average velocity of the fluid in the pipe. The friction factor, f, for a smooth pipe, has been calculated from the Blasius formula (valid for Re<100,000) given by Schlichting (Schlichting 1968):

$$f = \frac{0.316}{4(Re)^{1/4}} \tag{35}$$

where Re is the pipe Reynolds number.

Based on the previous equations, calculate the frequency at different Reynolds number. The calcualted relationship is shown in the following graph (Figure 7). The figure proves the correlation between the turbulent frequency and the Reynolds number. The turbulent frequency increses with the increaing Reynolds number. That is to say, increase the Reynolds number, the Stokes number and turbulence intensity will increase.

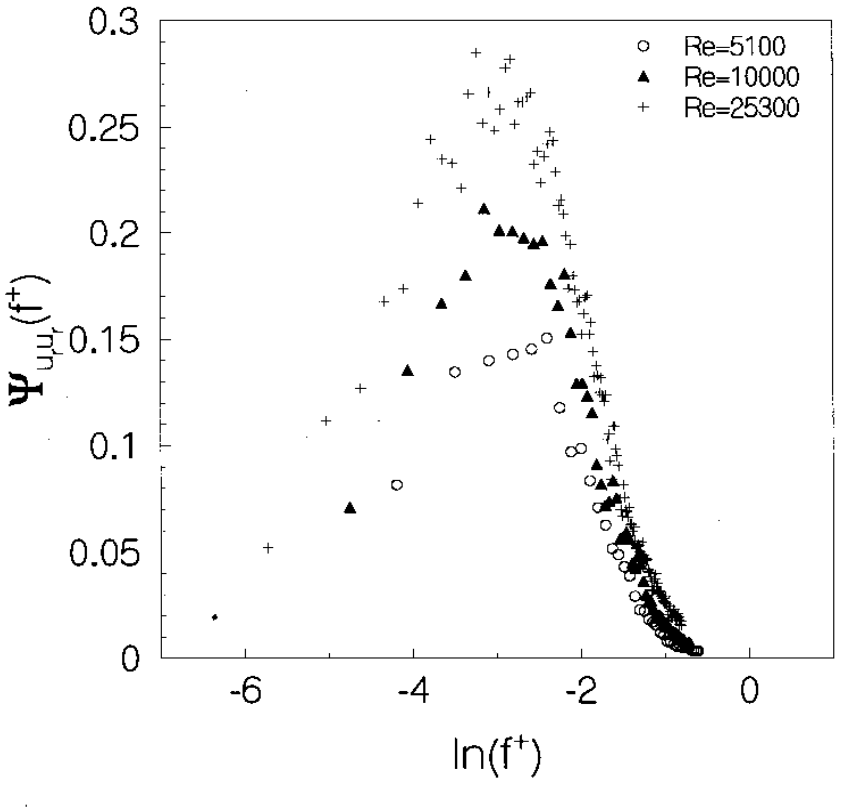

Figure 6 The power spectrum for the radical fluctuations at different Reynolds numbers by Toonder and Nieuwstadt

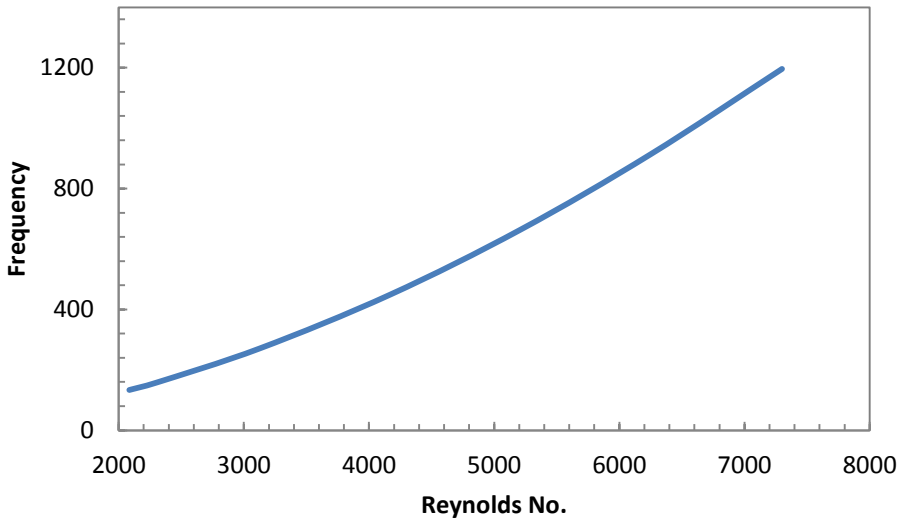

Figure 7 The calculated relationship between frequency and Reynolds number

In conclusion, the eddy impaction model can be described as the eddy impaction efficiency increases with increasing the Reynolds number or increasing particle size for a given gas velocity fluctuating environment.

4.2 Experiment Set Up

4.2.1 Experimental System

Usually, to investigate the ash deposition mechanism requires coal or biomass combustion in the pilot-scale facility and analysis of the ash either by measuring the amount of or taking pictures, etc. As mentioned before, inertial impaction is the dominant mechanism of ash deposition. However, for the small particles, eddy impaction was a significant influence on the deposition. So in this study we utilize gas to transport the particles and then measure the amount of deposition to explore the eddy impaction effects.

Figure 8 is a schematic diagram of the system used. In this investigation, small particles (printer toner, nano aluminum oxide particles and large aluminum oxide particles) provided

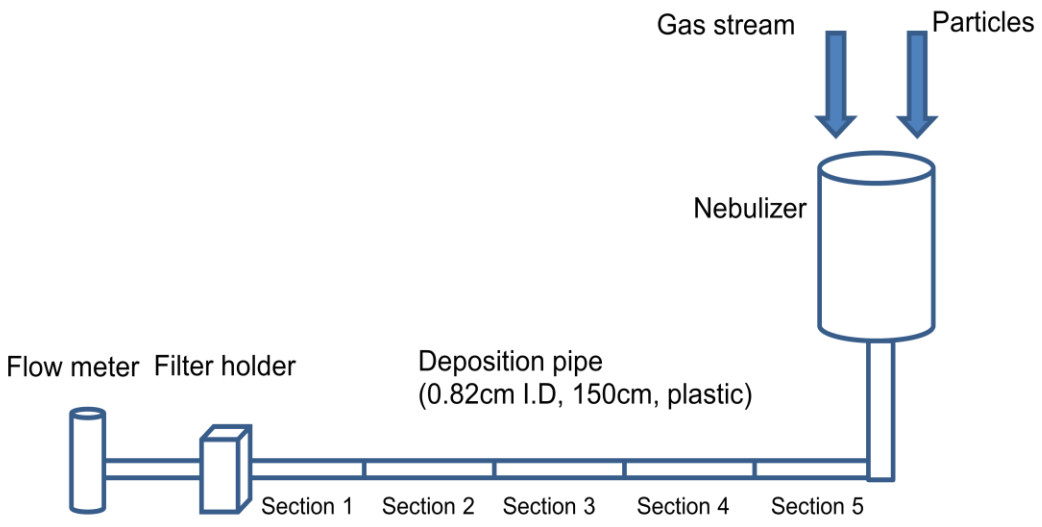

Figure 8 Experimental system

convenient and monodisperse fractions for analysis. The deposition experiment was run at room temperature and ambient atmosphere pressure conditions. A long (150 cm) and thin (0.82 cm dia.) plastic deposition pipe generated a fully developed flow. Please notice that the sections of deposition pipe are in reverse order because they follow the experiments remove sequence and the entrance section is not the first place but the last. A nebulizer [glass beaker or nebulizer (Rival 6-spend nebulizer 350 Watt motor)] help to introduce the particles. The gas stream transported particles through the tube over a range of Reynolds numbers. Compressed air and sulfur hexafluoride gases entrained the particles. SF_6 density exceeds that of air by a factor of about 5.2 and its viscosity is about 20% less than air, extending Reynolds numbers over 6 times relative to those in air alone and under otherwise similar conditions. Sulfur hexafluoride (SF_6) is more dense gas than air which can make a high Reynolds number and also easy to obtain.

The deposition tube comprises five 30 cm sections connected by larger flexible tubing that creates an air-tight seal. Separate sections make it possible to determine deposition in each individual section of pipe. A filter holder containing a 42.5 mm diameter filter paper (VWR Glass microfiber filter, 691, VWR North America Cat. No.28297-982) collected the particles that do not deposit on the tube surface. The flow transducer was calibrated with a standard precision rotameter. Generally, all the particles deposit on the tube prior to exiting the flow system. The amount of particles in each section was monitored over a range of flow rates.

4.2.2 Size Distribution Analysis

To investigate the different size effect on the deposition, different particles ((printer toner particles, nano aluminum oxide particles (Alfa-Aesar a Johnson Matthey company gamma-phase, 99+%, CAS#1344-28-1) and large aluminum oxide powder (alumnia, acid brockman activity,

Fisher Scientific Company, 40 mesh) are used to compare to each other. A Malvern Instruments' Spraytec (see Figure 9) was used to measure their size.

Malvern Instruments' Spraytec is a laser diffraction particle size system specifically designed to address the unique requirements of aerosol and spray droplet characterization across a wide range of industries and applications. The Spraytec provides *in-situ*, real-time droplet measurements in a fully validated package, giving accurate, reproducible results time.

Basic Settings of Spraytec: Measurement type: continuous

Sampling rate: 1s

Lens type: 300mm

Background duration: 10s

Figure 9 Malvern Spraytec Instrument

The size distributions of different particles are shown in the following tables. Based on the Table 4 and Figure 10, 50% of toner particles size less than 23 μm, 90% of toner particles size less than 40 μm, so estimate the average diameter of toner particles is around 25 μm which are called intermediate-sized particles. Similarly, according to Table 5 and Figure 10, 50% of alumina oxide particles size less than 487μm, 90% of that less than 708 μm, estimate the average diameter of aluminum oxide particles is 500 μm. After the SEM analysis (Figure 12 and Figure 13), the nano alumina oxide particles have an average diameter around 200 nm. The single nano aluminum oxide particle size is around 30 nm, however, the cluster particles diameter size is around 200 nm.

Table 4 Size distribution data of intermediate-sized particles

Standard Values:		
Trans = 90.7 (%)	Dv(10) = 10.94 (μm)	Span = 1.256
Cv = 39.11 (PPM)	Dv(50) = 22.69 (μm)	D[3][2] = 19.07 (μm)
SSA = 0.3146 (m^2/cc)	Dv(90) = 39.45 (μm)	D[4][3] = 24.22 (μm)

Trans: the transmission%.

Cv: the volume concentration. This is calculated in volume (%) from the Beer-Lambert law and is expressed in Parts Per Million (PRM).

SSA: specific surface area, the total area of the particles divided by the total weight.

Dv(x1): the percentiles, the size in microns which the specified % of the spray is smaller than. The commonest are Dv(10), Dv(50) and Dv(90), which are among the standard values.

D[x1][x2]: the moment means. The most commonly used are:

D[3][2]:the surface area moment mean diameter.

D[4][3]:the volume weighted or mass moment mean diameter.

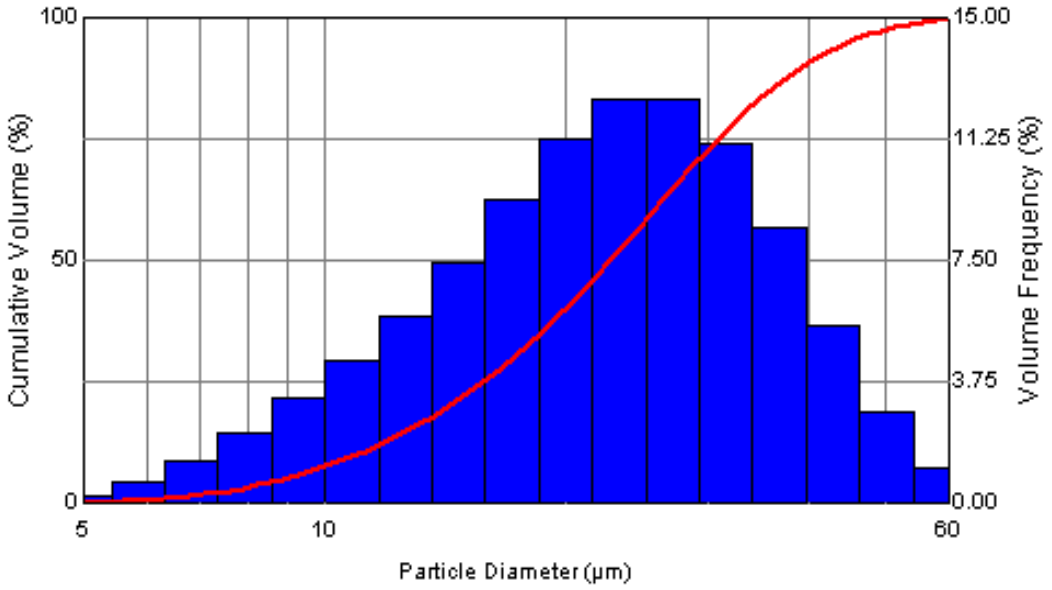

Figure 10 Size distribution of intermediate-sized particles

Table 5 Size distribution data of large aluminum oxide particles

Standard Values:		
Trans = 99.8 (%)	Dv(10) = 321.2 (µm)	Span = 0.7953
Cv = 20.94 (PPM)	Dv(50) = 486.8 (µm)	D[3][2] = 459 (µm)
SSA = 0.0131 (m²/cc)	Dv(90) = 708.3 (µm)	D[4][3] = 502.9 (µm)

4.2.3 Muffle Furnace Program Ramp Temperature Rate Setting

To remove crystal water, improve the percentage of oxide metal and enhance the physical properties of the particles, a muffle furnace was applied to the aluminum oxide particles.

Temperature rate setting:

$$20^{\circ}C \xrightarrow{12\text{min}} 120^{\circ}C \xrightarrow{20\text{min}} 200^{\circ}C \xrightarrow{50\text{min}} 700^{\circ}C \xrightarrow{600\text{min}} 700^{\circ}C$$

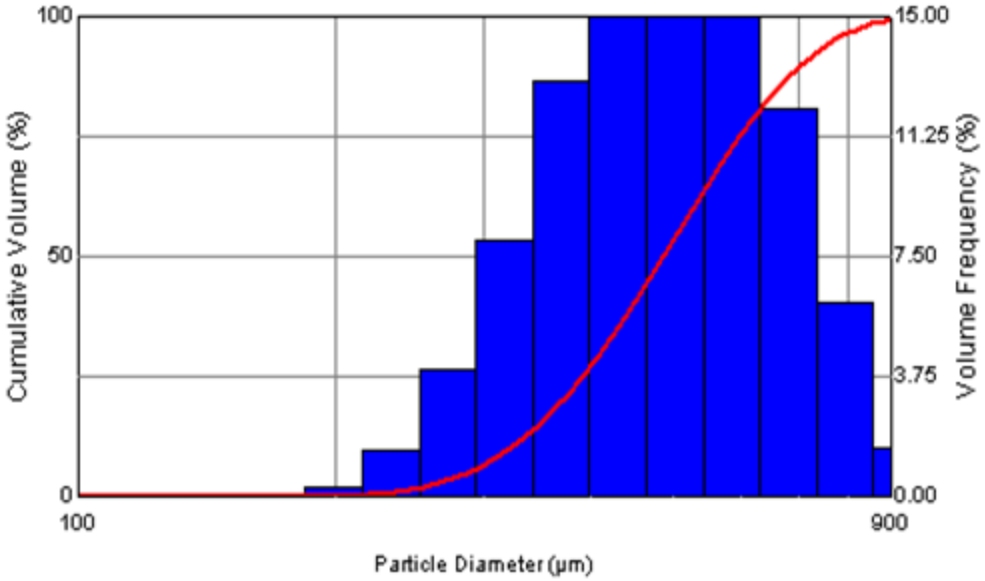

Figure 11 Size distribution of large aluminum oxide particles

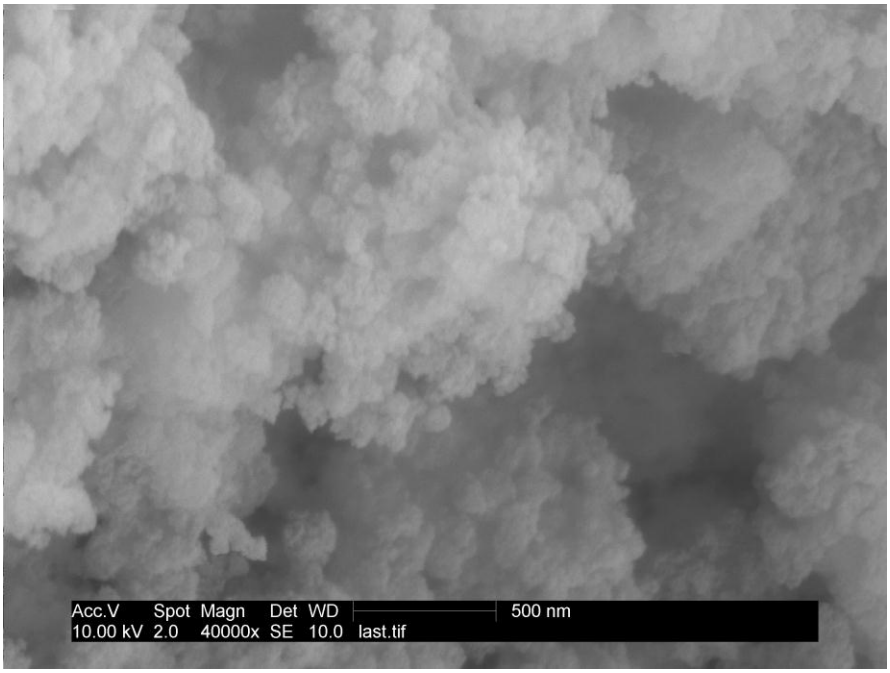

Figure 12 SEM map of nano aluminum oxide particles

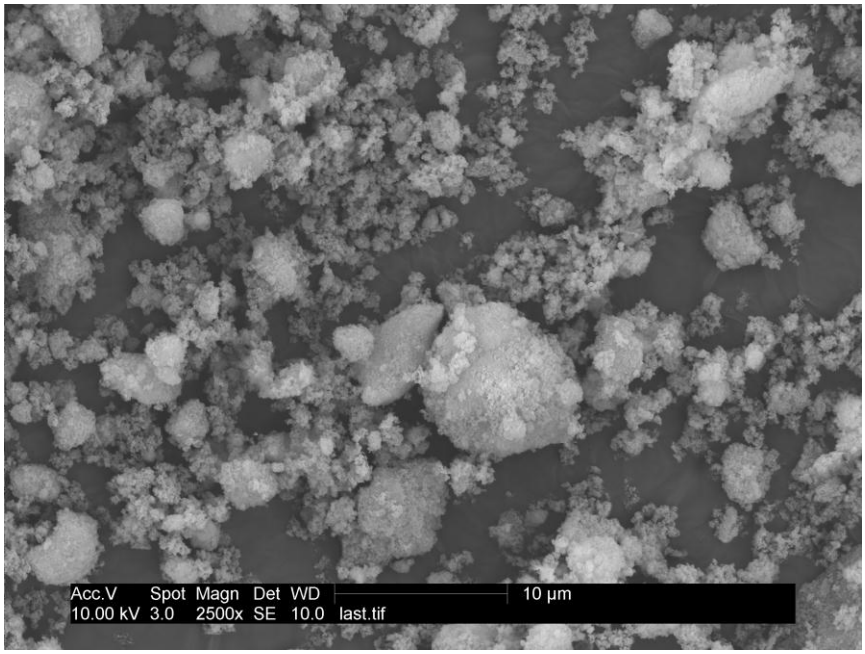

Figure 13 SEM map of nano aluminum oxide particles in large scale

5 RESULTS AND DISCUSSION

Several experimental runs were performed using the equipment and apparatus described. Toner particles are used for most of experiments. Different size of aluminum oxide particles indicates the effect of diameter on the deposition rates and mechanisms. The different types of particles were fed at different rates under different gas conditions. This section discusses the comparison between deposition rates based on the experimental data for both feed rates and particle type. Following that is a discussion of the application of an ash deposition model to the experimental data obtained in this investigation. The objective of the application was to reveal the eddy impaction mechanism.

5.1 Calculation Method

The deposition velocity is calculated from the equation given by Sehmel (Sehmel 1973):

$$V = \frac{Q}{\pi DL} \ln\left(\frac{1}{P}\right) \tag{36}$$

where Q is the volumetric flow rate, D is the i.d. of the deposition pipe, L is the length of the section, and P is the fractional penetration through the individual section.

To consider the entrance length effect, Reynolds number will be focused on because it is the only parameter to affect that (Frank 2003). If,

Le=f(d,V,ρ,μ), $V=\frac{Q}{A}$

Then

$$\frac{L_e}{d} = g\left(\frac{\rho v d}{\mu}\right) = g(Re) \tag{37}$$

For laminar flow, the accepted correlation is

$$\frac{L_e}{d} \approx 0.06Re \tag{38}$$

The maximum laminar entrance length, at $Re_{d,crit}$ of 2300, is L_e= 138 d, where d is diameter of the tube. In this system d=0.82 cm, L=150 cm, thus L_e=113 cm. In turbulent flow the approximation for smooth walls,

$$\frac{Le}{d} \approx 4.4Re_d^{1/6} \tag{39}$$

Some computed turbulent entrance lengths are calculated in Table 6.

Table 6 Some computed turbulent entrance length based on Reynolds number

Re	4170	5210	6250	7300	8350
L_e (cm)	17.65	18.32	18.88	19.38	19.82

Table 6 indicates that the entrance effect may only affect the section near the entrance. However, even in laminar flow, sections 1 and 2 (which are the farthest sections away from entrance) are fully developed, and therefore sections 1 (150 cm) and 2 (120 cm) will be investigated.

5.2 Effects of Gas

To verify the eddy impaction model, we have to run different rates flow. Figure 14 is a plot of results collected in the experiments with intermediate-sized particles, compressed air and a beaker as the delivering container. The system is restricted when Reynolds number is 2500 thus

the flow is not turbulence at this situation. The curve has a decrease shape, however, its increasing trend still accordance with the eddy impaction model. For a higher Reynolds number a more dense gas must be used. Sulfur hexafluoride was used because under standard conditions it is very dense.

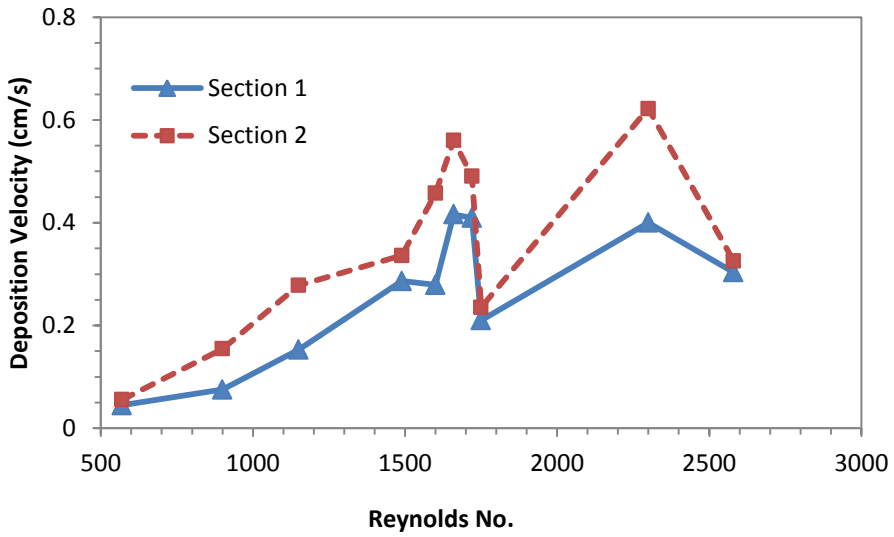

Figure 14 Plot of deposition velocity vs. Re at compressed air condition

Sulfur hexafluoride (SF_6) is an inorganic, colorless, odorless, non-toxic and non-flammable gas. SF_6 has an octahedral geometry, consisting of six fluorine atoms attached to a central sulfur atom. It is a hypervalent molecule. Typical for a nonpolar gas, it is poorly soluble in water but soluble in nonpolar organic solvents. It is generally transported as a liquefied compressed gas. It has a density of 6.12 g/L at sea level conditions, which is considerably higher than the density of air.

Figure 15 is the deposition velocities at SF_6 condition. It is illustrated that SF_6 can largely improve the gas turbulence and makes it easy to reach a Reynolds number of 8000. However, the graph is oscillating. This indicates the experiment system is not stable.

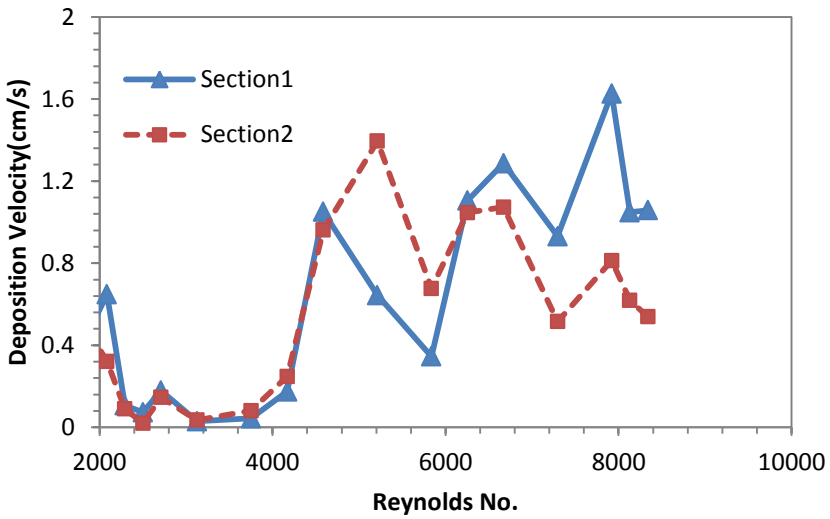

Figure 15 Plot of deposition velocity vs. Re at SF_6 condition

The nebulizer generates continues vortex which can improve gas mix. Then a nebulizer is used to decrease the variation.

Figure 16 is the depostion velocity at different secions with nebulizer systerm under compressed air conditions. The deposition velocities at section 1 (150 cm) and 2 (120 cm) are close and show small variation. It verifies the improvement of adding a nebulizer to the system and illustrates nebulizer can improve the stability of the system and significantly decrease the variation. A nebulizer will be applied to subsequent experimental runs.

5.3 SF_6 and Nebulizer Used

Table 7 Sample intermediate-sized particle deposition data for the deposition pipe shows the results for a typical experimental run. The quantity of intermediate-sized particles deposited on the individual section is shown in column 1 and column 2. From these values, the fraction of particles penetrating through each individual section (i.e. fraction of material not deposited in the section) is calculated. Calculations are from the method explained in section 5.1.

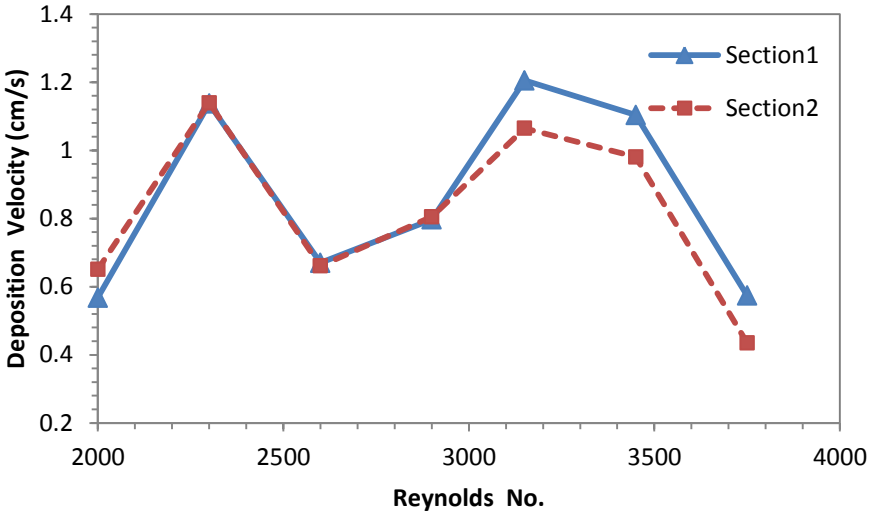

Figure 16 Plot of deposition velocity vs. Re at compressed air condition with nebulizer system

Table 7 Sample intermediate-sized particle deposition data for the deposition pipe

	Deposited in section (g)	Penetrated in section (g)	Fractional penetration in section	Deposition velocity for section (cm/s)	Average deposition velocity calculated from sections 1-4
Connection	0.1241				
Section5(30cm)	0.2087	1.204	0.852	0.246	
(Entrance)					
Section4(60cm)	0.3507	0.8533	0.709	0.54	
Section3(90cm)	0.2566	0.5967	0.699	0.552	0.611
Section2(120cm)	0.2023	0.3944	0.661	0.671	
Section1(150cm)	0.1383	0.2561	0.649	0.684	
(Exit)					
Filter paper	0.132				
sum	1.4127	1.4127			
	Flow rate=	122.7 cm^3/s	Re=	7300	
	D=	0.82 cm	L=	30 cm	

Since the fractional penetrations between sections 1 and 4 are essentially constant, the corresponding deposition velocities based on these penetration values vary by not more than 10 percent from the average deposition velocity of 0.611 cm/sec. The low deposition velocity for section 5 near the entrance to the deposition pipe is expected because of the finite transition length needed for the flow to become fully turbulent.

Figure 17 indicates the deposition velocity shows a very rapid increase until Reynolds number reaches 6000, where it peaks. After 6000 it displays only moderate changes. The deposition velocities at section 1 and section 2 almost look the same when the Reynolds number is lower than 2300. In the transition region they are quite different. In the turbulence region, starting from 5000, they begin to close again. This indicates that the system is stable because section 1 and section 2 are at different places. However, the deposition velocities in transition area are random. Generally, this increasing trend follows Figure 5 eddy impaction increases with the increasing the turbulence.

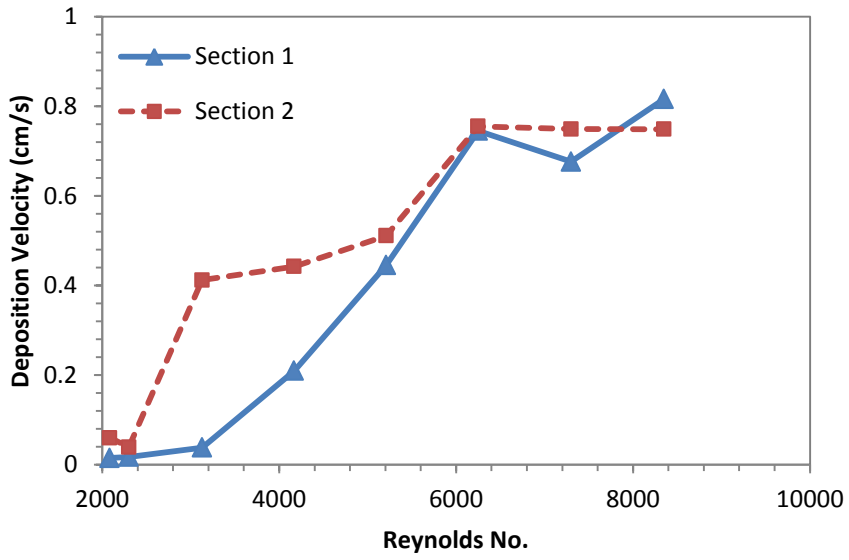

Figure 17 Experimental relationships between deposition velocities at different Reynolds number in SF_6 condition

5.4 Compare the Experimental Data in Nebulizer and Without Nebulizer

Typically 3-6 duplicate runs determine the reproducibility of the experiments and error bars of the experimental measurements. The error bars in the following charts are ± σ, or one standard deviation, based on these replicates. The 95% confidence intervals typically are about the same size, depending on the number of replicates.

5.4.1 Comparison at Laminar Region

At the lowest Reynolds numbers (2300), the flow is nearly laminar and eddy impaction rates are slow but not zero. Experiments with nebulized particles (Figure 18) produce deposition velocity standard deviations in each section of the tubing of 0.0487, 0.0177, 0.0076, 0.0138, and 0.010, respectively, and the sum of all sample standard deviations indicates the standard deviation of the system is 0.0980. The average standard deviation is 0.019, or in another words, the system coefficient variation is 1.9%.

The variation of deposition velocity with length is consistent with boundary layer development. Near the tubing entrance, the boundary layer is very thin and the deposition velocity is correspondingly high, with decreases as the boundary layer becomes thicker. Eventually, the boundary layer thickness becomes constant. Empirical correlations estimate this entry length, as is included in the figure. After the entry length, the deposition velocity should be essentially constant with respect to distance, consistent with the data.

Without the nebulizer (Figure 19), the standard deviations at each distance are 0.1564, 0.1106, 0.0234, 0.0356 and 0.020, respectively, and the sum of all sample standard deviations is 0.3461. This is 71.54% larger than the sum standard deviation with nebulizer. The average standard deviation is 0.0692, producing a system coefficient of variation of 6.92%, which is 72.25% larger than the average standard deviation with nebulizer. The error bars vary less from

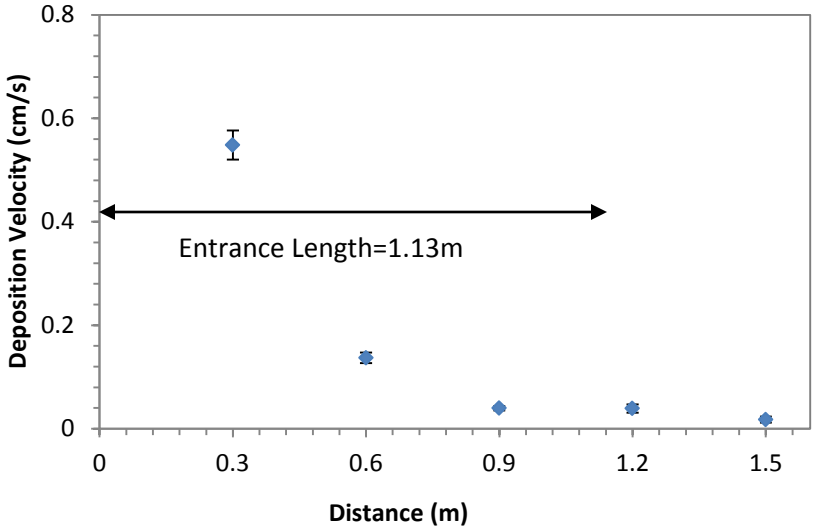

Figure 18 Plot of deposition velocity at different places in duplicate runs when Re=2300 with nebulizer

section to section in the nebulized system. In the laminar region, the entrance length is 1.13 m, thus the particle deposition velocities keep almost constant at the distance at 1.2 m and 1.5 m when the flow is fully developed, the deposition velocity is calculated the average of those two points.

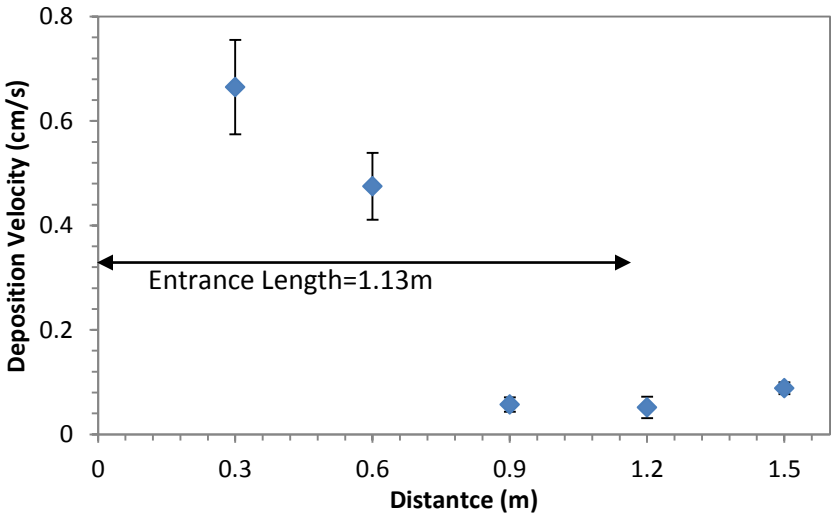

Figure 19 Plot of deposition velocity at different places in different runs when Re=2300 without nebulizer

5.4.2 Comparison at Turbulent Region

At the highest Reynolds numbers (> 6000), the flow is fully turbulent and eddy impaction rates are more rapid than in the laminar regime. In the nebulizer system (Figure 20), the standard deviations at each distance when Re are 6250 is 0.0379, 0.0575, 0.0079, 0.0042 and 0.0642, respectively, and the summation of all sample standard deviations indicates the standard deviation of the system is 0.1718. The average of sample standard deviation is 0.0344, or in another words, the variance of the system is 3.44% in total. Without the nebulizer (Figure 21), the standard deviations at each distance are 0.0246, 0.0817, 0.1527, 0.0382 and 0.0984 respectively. The summation of all sample standard deviation is 0.6171, which is 72.16% larger than the standard deviation with nebulizer. The average of the sample standard deviations is 0.0791, which is 35.6% larger than that with nebulizer. The error plots provide smaller variance in system with nebulizer. The longest entrance length is 0.19 m, so at this flow rate, we can use the average of the last four points deposition velocities as the total. The data consistently show

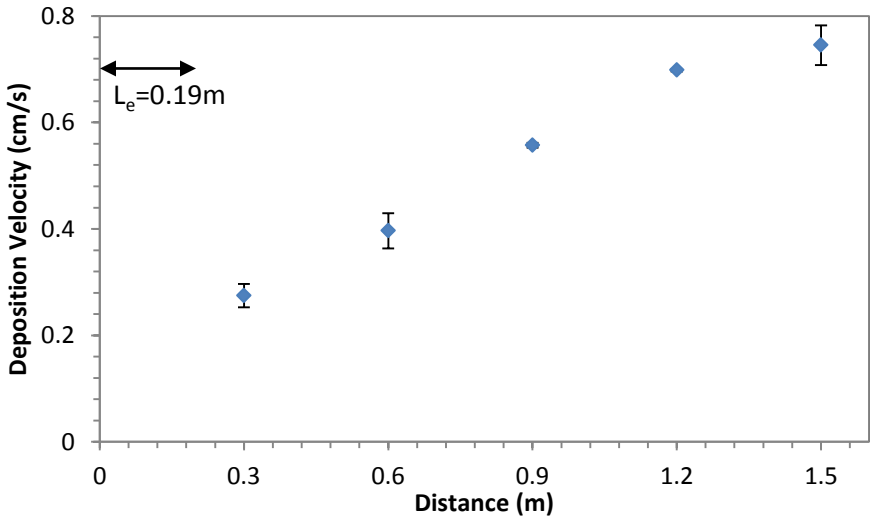

Figure 20 Plot of deposition velocity at different sections in different runs when Re=6250 with nebulizer

the deposition velocity increasing with increasing distance, which is neither expected nor easily explained but is possibly related to the effects of particle accumulation in the boundary layer in previous sections of the tubing.

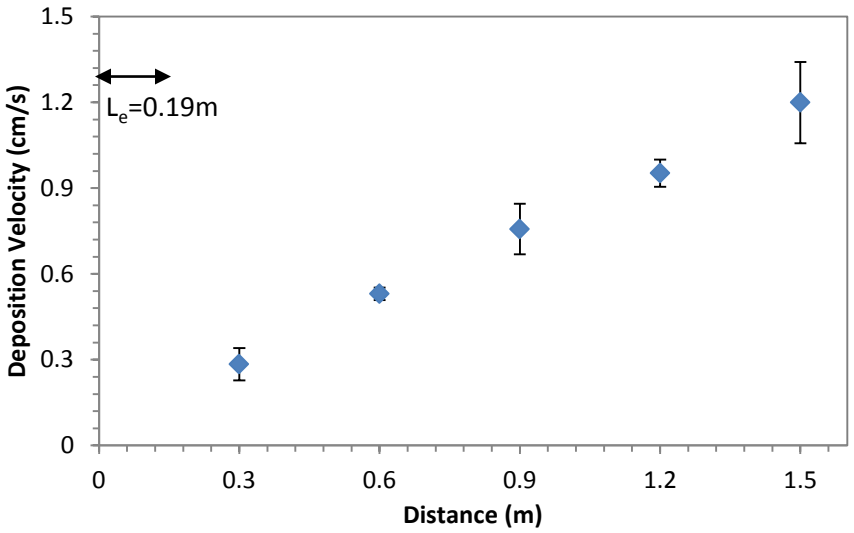

Figure 21 Plot of deposition velocity at different section in duplicate runs when Re=6250 without nebulizer

5.4.3 Comparison at Transition Region

At intermediate Reynolds numbers, the fluid is in a transition regime that is neither fully turbulent nor laminar. Flow patterns in such regimes are known to be turbulent. In the nebulized system (Figure 22), the standard deviations at each distance when Re are 3130 are 0.2249, 0.0312, 0.2804, 0.0449 and 0.0072, respectively, and the sum of all sample standard deviation indicates the standard deviation of the system is 0.5886. The average of sample standard deviation is 0.1177, or in another words, the variance of the system is 11.77% in total.

Without the nebulizer (Figure 23), the standard deviations at each distance are 0.1100, 0.0382, 0.1037, 0.1533, and 0.0984, respectively. The summation of all sample standard

deviation is 0.5411; quite close the standard deviation with nebulizer. The average standard deviation is 0.101, which is close with that of the system with a blender. This illustrated that in the transit region, either with nebulizer, the deposition velocity is a little random.

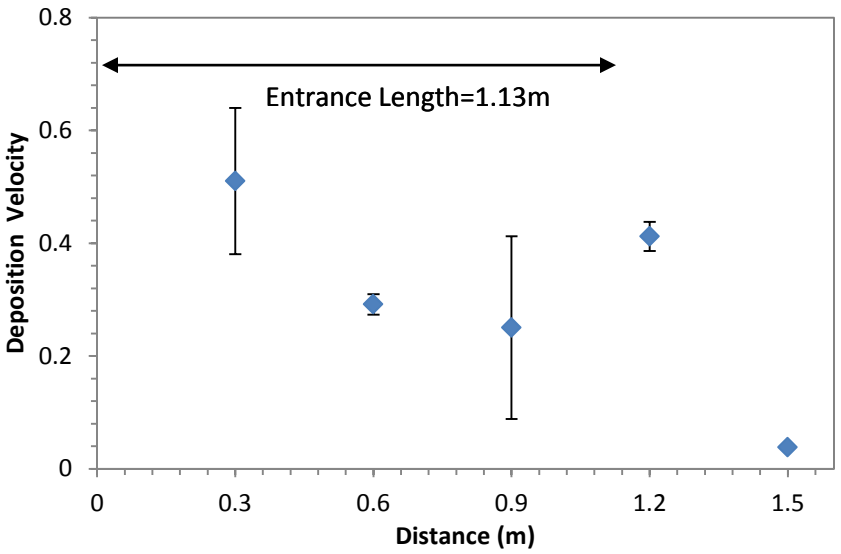

Figure 22 Plot of deposition velocity at different sections in different runs when Re=3130 with nebulizer

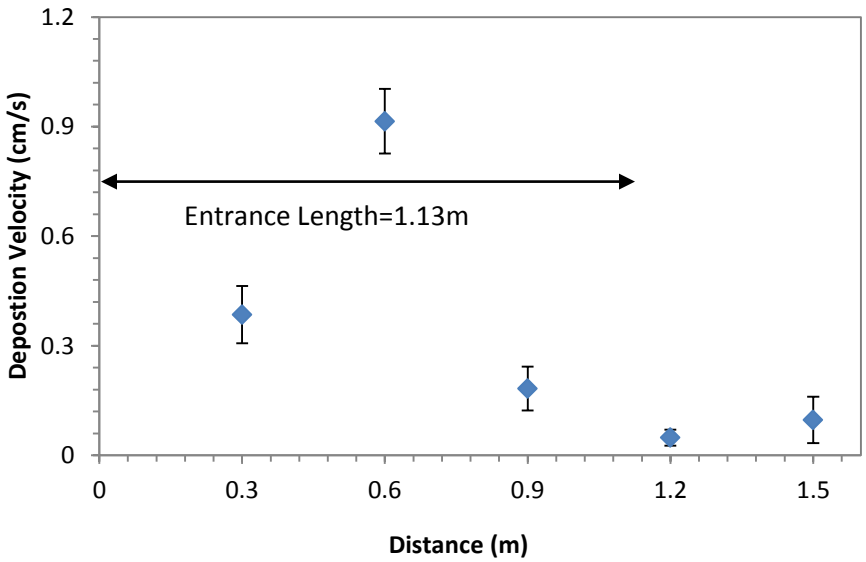

Figure 23 Plot of deposition velocity at different sections in different runs when Re=3130 without nebulizer

The comparisons show that the variances of the nebulizer system are 1.9% and 3.44% at laminar and turbulent regions, proving that the maximum difference of duplicate runs is less than 4 percent (Figure 18 and Figure 20). This is around 72% lower than that of a system without nebulizer, thus we can concluded that a nebulizer can largely improve the stability of the system, giving only small variations in laminar and turbulent region. However, the values in Figure 22 are more random because when Re= 3130 the system is in the transit region and the particles' movements are more complex.

Figure 24 is the relationship between deposition velocity and different position of the pipe at different Reynolds number. Considered the entrance length effect, laminar and transit region will consider the last two point which is section 1 (150 cm) and section 2 (120 cm). The deposition velocities at last two sections in laminar and turbulent region are keep constant which illustrate the data are creditable. It clearly shows with the Reynolds number increased, more particles will deposit and they prone to deposit further positions. However, in transit region, it still need further investigated.

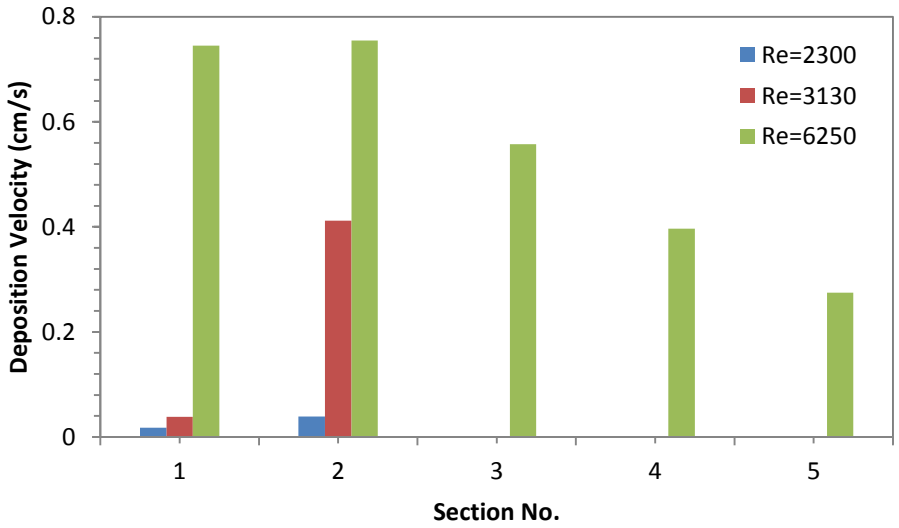

Figure 24 Compare deposition velocities at different sections using toner particles

Table 8 is a summary of the experimental results for average deposition velocity at different Reynolds numbers. A dimensionless relaxation time of the particles, τ_+ , is defined by Liu and Agarwal (Liu 1974) as

$$\tau_+ = \frac{\tau v_*^2}{\nu} \tag{40}$$

and a dimensionless deposition velocity defined as:

$$V_+ = \frac{V}{v_*} \tag{41}$$

here ν is the kinematic viscosity of gas, τ is the particle relaxation time, and v_* is the friction velocity of the turbulent flow.

Table 8 Intermediate-sized particle deposition in 0.82 cm plastic pipe

Reynolds No.	Average velocity of gas	Fraction velocity (v*)	Dimensionless particle relaxation time, τ+	Average deposition velocity, V(cm/s)	Dimensionless deposition velocity, V+
2085	0.664	0.051	0.0106	0.037	0.0074
2300	0.73	0.055	0.0126	0.028	0.0051
3130	0.996	0.072	0.0216	0.225	0.0311
4170	1.328	0.093	0.0358	0.326	0.0350
5210	1.66	0.113	0.0529	0.478	0.0422
6250	1.992	0.133	0.0728	0.65	0.0459
7300	2.324	0.152	0.0953	0.712	0.0469
8350	2.656	0.171	0.120	0.782	0.0458

For spherical particles in the Stokes regime, the relaxation time is the inverse of the previously discussed parameter β,

$$\tau = \frac{\rho_p d_p^2 C_C}{18\mu_g} = \frac{1}{\beta} \tag{42}$$

where ρ_P is the particle density, μ is the viscosity of the gas, and C is the previously discussed Cunningham slip correction. The friction velocity defined by Liu and Agarwal (Liu 1974) is

$$v_* = (f/2)^{1/2}\bar{u} \tag{43}$$

where $\bar{u}$ is the average velocity of the fluid in the pipe. The friction factor, f, for a smooth pipe, has been calculated from the Blasius formula (valid for Re<100,000) given by Schlichting (Schlichting 1968):

$$f = \frac{0.316}{4(Re)^{1/4}} \tag{44}$$

where Re is the pipe Reynolds number.

Figure 25 illustrates experimental results of the dimensionless deposition velocity, V+, increasesing rapidly with increasing particle relaxation time, τ+, reaching a peak around 0.047 at a τ+ value of approximately 0.10. After that, V+ shows a slightly decreasing trend.

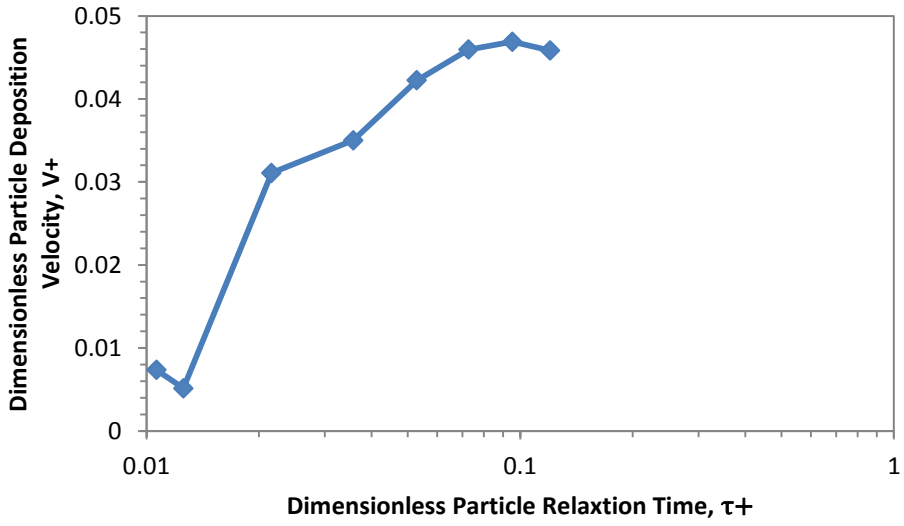

Figure 25 Experimental relationship between the dimensionless particle deposition velocity, V+ , and the dimensionless particle relaxation time, τ+

5.5 Measured Nano Aluminum Oxide Particles Deposition Rates

Aside from turbulence, particle diameter also will affect the deposition rate. To demonstrate this point, this part of the discussion is focused on the nano aluminum oxide particles.

The standard deviations at each distance when Re is 2300 (Figure 26) are 0.01119, 0.02414, 0.03295, 0.03100 and 0.03829, respectively, and the sum of all sample standard deviation indicates the standard deviation of the system is 0.1376. The average standard deviation is 0.0275, or in another words, the variance of the system is 2.75% in total. Considering the longest entrance length, we can average the last two points as the total deposition velocity at this flow rate.

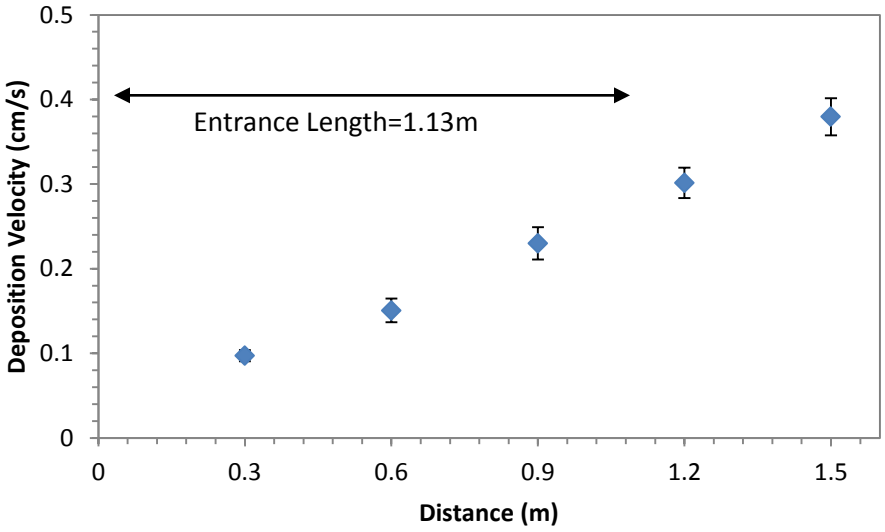

Figure 26 Plot of deposition velocity at duplicate runs when Re=2300 using nanoparticles

The standard deviations at each distance when Re is 3100 (Figure 27) are 0.08442, 0.1358, 0.1227, 0.05313and 0.03106, respectively, and the sum of all sample standard deviation indicates the standard deviation of the system is 0.4271. The average standard deviation is

0.0854, or in another words, the variance of the system is 8.54% in total. The error plot shows large variance at different places when duplicate runs at transit region. The complex flow rate generates this problem.

The standard deviation at each distance when Re are 6250 (Figure 28) is 0.05234, 0.04916, 0.03885, 0.01975 and 0.01311, respectively, and the sum of all sample standard deviation indicates the standard deviation of the system is 0.1732. The average standard deviation is 0.0346, in another words, the variance of the system is 3.46% in total. Since the deposition velocity at 1.5 m is quite larger than the other points (see Figure 30 and following explains), we average the section 2 to 5 as the deposition velocity at this flow rate. As follow the toner particles trend, at laminar and turbulent flow area, the variance is about 3% in average which suggests the system is stable.

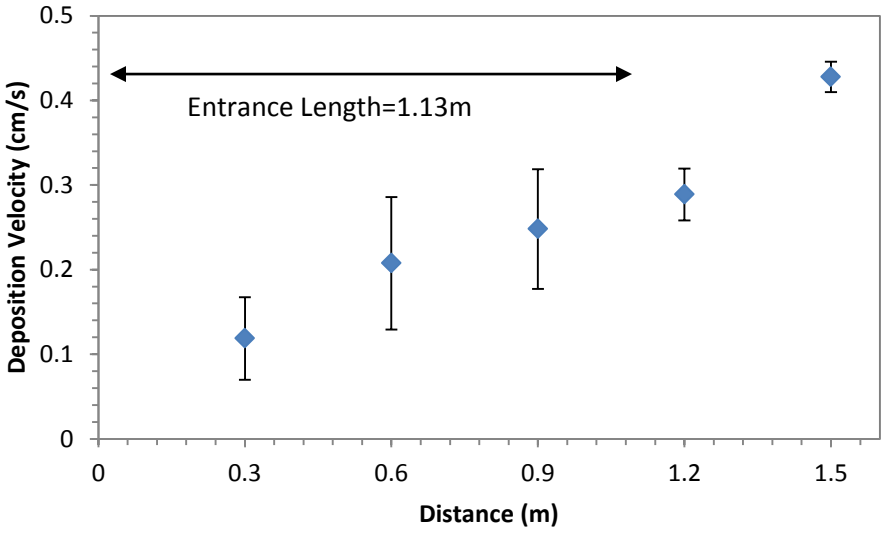

Figure 27 Plot of deposition velocity at duplicate runs when Re=3100 using nanoparticles

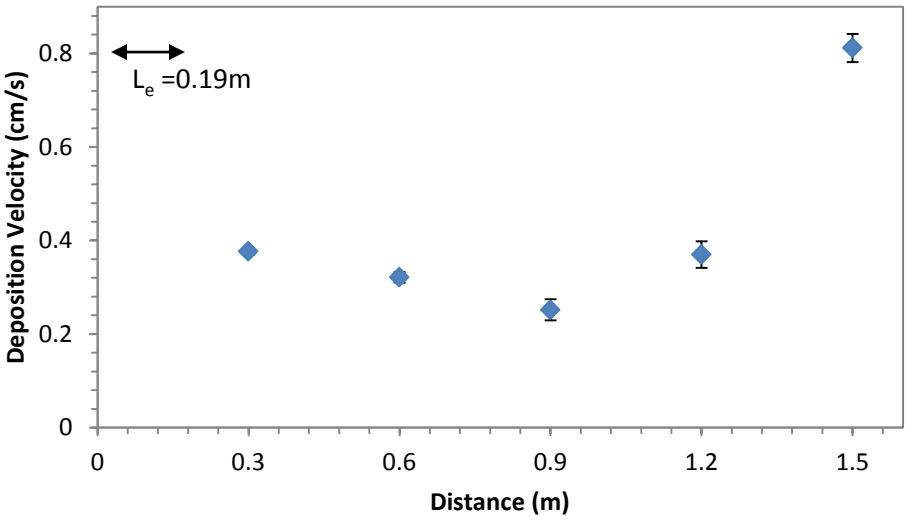

Figure 28 Plot of deposition velocity at duplicate runs when Re=6250 using nanoparticles

Figure 29 is the relationship between deposition velocity and different position of the pipe at different Reynolds number using nano particles. It follows the toner particles plot in

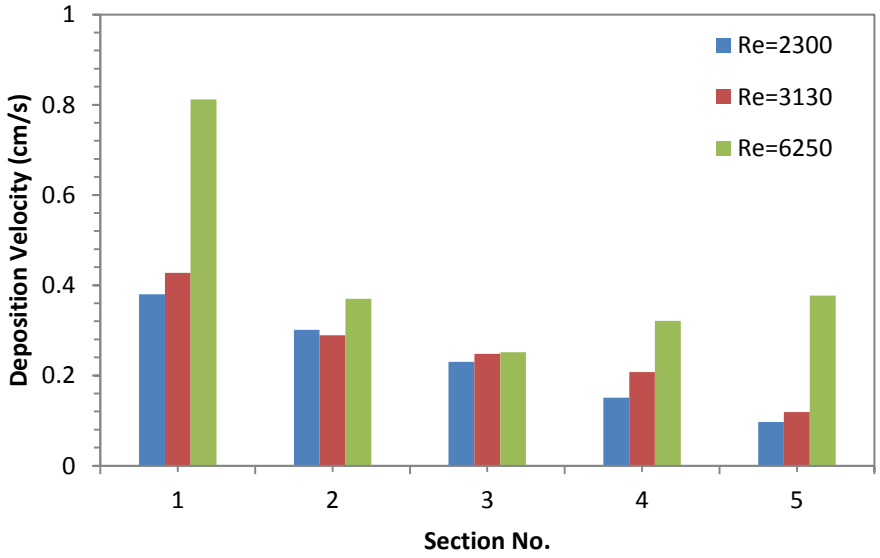

Figure 29 Compare deposition velocities at different sections using nanoparticles

Figure 25 illustrate particles increase deposit with the Reynolds number increased and they also prefer to deposit further from the entrance. Following the method talked in section 5.1, sections 1 (150cm) and 2 (120cm) are investigated for comparison. Figure 30 is the relationship between the nanoparticles' deposition velocity vs. Reynolds number. The blue line is deposition velocity in section1 which near the exit and the red line is deposition velocity in section 2. It illustrates that with the increased Reynolds number, particles deposit improves. This means that it was more difficult for the nanoparticles to exit from the deposition tube, and more and more particles deposited in the last section. For these tiny particles, the entrance effects are very small. The deposition velocity in the exit section, however, is more than 100% larger than the deposition velocity in other sections. Considering this situation, the average deposition velocity was calculated from section 2 to 5 in the turbulent region.

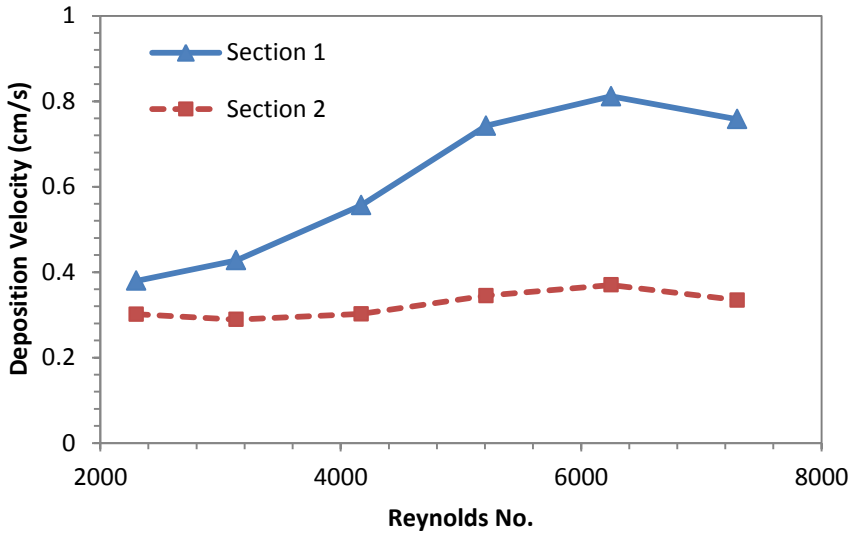

Figure 30 Plot of deposition velocity at different Reynolds numbers in section 1 and 2 using nanoparticles

Table 9 and Table 10 show the results for a typical experiment run when the Reynolds number was 3100 and 6250, respectively. Notice that the fractional penetrations are close from section 2 to 5, especially section 2 to 4, which further illustrate the previous consideration is good estimation to calculate the average deposition velocity.

The summary of the experimental results is shown in Table 11. The average deposition velocity shown is based on the average penetration through 30cm long section comprised of section 2-5.

Table 9 Sample nanoparticle deposition data for deposition pipe at Re=3100

	Deposited in section (g)	Penetrated in section (g)	Fractional penetration in section	Deposition velocity for section (cm/s)	Average deposition velocity calculated from sections2-5
Connection	0.0418				
Section5 (Entrance)	0.3184	0.7988	0.715	0.2116	
Section4	0.3318	0.467	0.5846	0.3372	
Section3	0.1464	0.3206	0.6865	0.2242	0.2503
Section2	0.1014	0.2192	0.6837	0.228	
Section1 (Exit)	0.1233	0.0959	0.4375	0.4338	
Filter paper	0.0959				
sum	1.1172	1.1172			
	Flow rate=	52.57 cm^3/s	Re=	3100	
	D=	0.82 cm	L=	30 cm	

Figure 31 is a plot of the experimental results given in Table 11. The dimensionless deposition velocity, V+, is seen to increase from 0.015 to around 0.03 with increasing particle relaxation time, τ+, to around 0.000004. Although it has a little oscillation, this trend is similar to the toner particle dimensionless graph, and the maximum dimensionless deposition velocity is smaller than the toner particles which is approaching 0.05.

Table 10 Sample nanoparticle deposition data for deposition pipe at Re=6250

	Deposited in section(g)	Penetrated in section(g)	Fractional penetration in section	Deposition velocity for section(cm/s)	Average deposition velocity calculated from sections2-5
Section5 (Entrance)	0.3922	0.5488	0.5832	0.3787	
Section4	0.1218	0.427	0.7781	0.3155	
Section3	0.0912	0.3358	0.7864	0.292	0.3452
Section2	0.0911	0.2447	0.7287	0.3945	
Section1 (Exit)	0.1248	0.1199	0.49	0.8096	
Filter paper	0.1199				
sum	0.941	0.941			
	Flow rate=	105.2 cm^3/s	Re=	6250	
	D=	0.82 cm	L=	30 cm	

Table 11 Aluminum oxide nanoparticle deposition in 0.82 cm i.d. plastic pipe

Reynolds No.	Average velocity of gas	Fraction velocity(v*)	Dimensionless particle relaxation time, τ+	Average deposition velocity,V(cm/s)	Dimensionless deposition velocity, V+
2085	0.664	0.051	5.407E-06	0.079	0.0155
2300	0.73	0.055	2.558E-06	0.106	0.0192
3130	0.996	0.072	1.099E-06	0.169	0.0233
4170	1.328	0.093	1.819E-06	0.229	0.0246
5210	1.66	0.113	2.688E-05	0.338	0.0290
6250	1.992	0.133	3.699E-05	0.397	0.0299
7300	2.324	0.152	4.842E-05	0.478	0.0314

5.6 Measured Large Alumina Oxide Particles Deposition Rates

To verify the effects of size on eddy impaction, different sized particles (500 μm aluminum oxide particles) were used.

The standard deviations at each distance when Re is 2300 (see Figure 32) are 0.01355, 0.01818, 0.02303, 0.01034 and 0.00932, respectively. The sum of all sample standard deviation

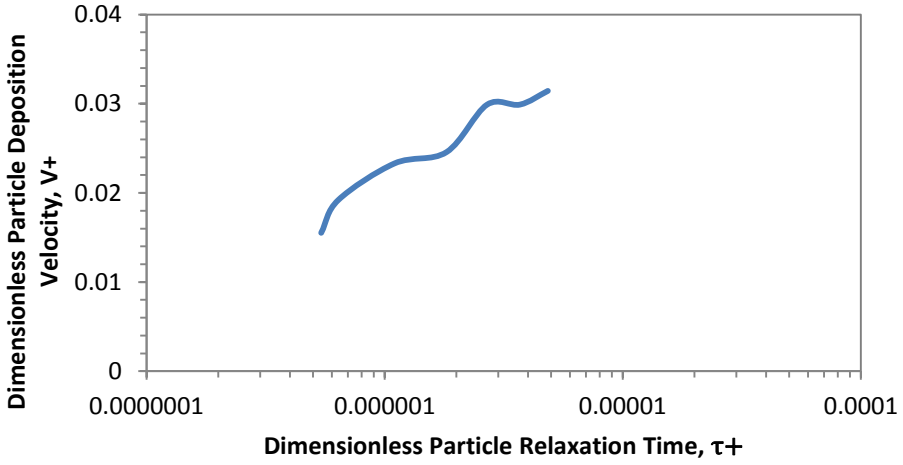

Figure 31 Experimental relationships of nanoparticles between the dimensionless particle deposition velocity, V+, and the dimensionless particle relaxation time, τ+

indicates the standard deviation of the system is 0.0744. The average standard deviation is 0.0149, or in another words, the variance of the system is 1.49% in total. From Figure 32 error plot shows smaller variance of deposition velocity at 1.2 m and 1.5 m, which are in fully developed regions.

The standard deviation at each distance when Re is 3100 (see Figure 33) is 0.04195, 0.1145, 0.05768, 0.03064and 0.04341 respectively. The summation of all sample standard deviation indicates the standard deviation of the system is 0.2882. The average of sample standard deviation is 0.0576, or in another words, the variance of the system is 5.76% in total.

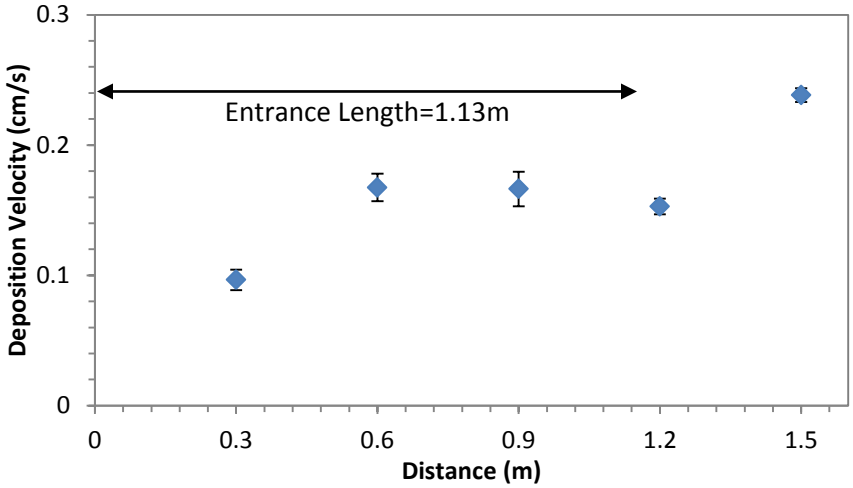

Figure 32 Plot of deposition velocity at duplicate runs when Re=2300 using large particles

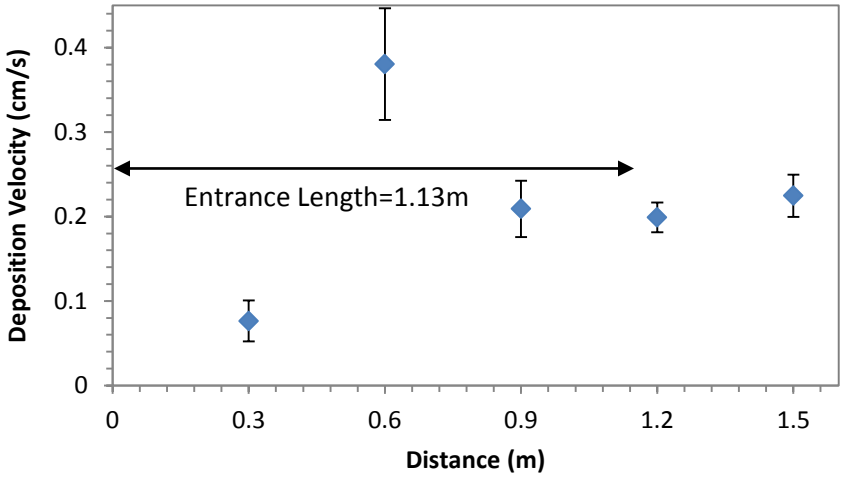

Figure 33 Plot of deposition velocity at duplicate runs when Re=3100 using large particles

The standard deviation at each distance when Re is 6250 (see Figure 34) is 0.03867, 0.02904, 0.03022, 0.01460 and 0.02628 respectively, and the summation of all sample standard deviation is 0.104. The average of sample standard deviation is 0.0208, or in another words, the variance of the system is 2.08% in total.

Following the toner and nanoparticles trend at laminar and turbulent flow area, the variances are 1.49% and 2.08%, which agrees with the conclusion made before that the nebulizer system is stable. Additionally, the standard deviation in the transition region is 5.76%, which is also small and indicate the results are reliable. Following the previous method talked in section 5.1, sections 1 and 2 were investigated for comparison. The entrance effect was large for the large aluminum oxide particles, and the average deposition velocity is calculated for sections 1 and 2.

The summary of the experimental results is shown in Table 13. The average deposition velocity shown is based on the average penetration through 30 cm long section comprised of sections1 and section 2

Table 12 shows the result for a typical experimental run. The fractional penetrations are stable in section 1 and section 2 which demonstrate that the estimation those points as the average data is convincing.

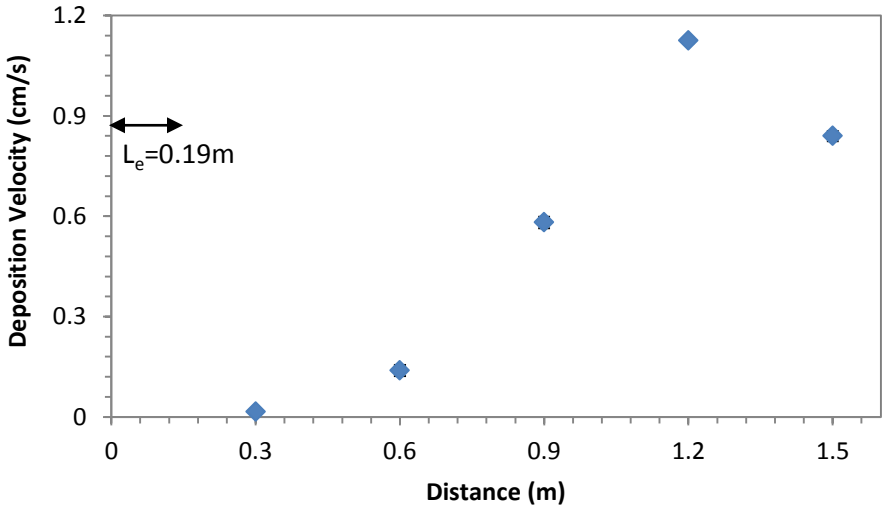

Figure 34 Plot of deposition velocity at duplicate runs when Re=6250 using large particles

The summary of the experimental results is shown in Table 13. The average deposition velocity shown is based on the average penetration through 30 cm long section comprised of sections1 and section 2

Table 12 Sample large particle deposition data for deposition pipe

	Deposited in section(g)	Penetrated in section(g)	Fractional penetration in section	Deposition velocity for section(cm/s)	Average deposition velocity calculated for sections1-2
Section5 (Entrance)	0.1394	6.8184	0.98	0.0266	
Section4	0.5165	6.3019	0.9242	0.1058	
Section3	2.8593	3.4426	0.5463	0.7991	
Section2	1.8967	1.5459	0.4491	1.1121	0.9763
Section1 (Exit)	0.7138	0.8321	0.5383	0.8404	
Filter paper	0.8321				
sum	6.9578	6.9578			
	Flow rate=	105.15 cm^3/s	Re=	6250	
	D=	0.82 cm	L=	30 cm	

Table 13 Large aluminum oxide particle deposition in 0.82 cm i.d plastic pipe

Reynolds No.	Average velocity of gas	Fraction velocity(v*)	Dimensionless particle relaxation time, τ+	Average deposition velocity,V(cm/s)	Dimensionless deposition velocity, V+
2085	0.664	0.051	3.380	0.021	0.0042
2300	0.73	0.055	3.990	0.196	0.0355
3130	0.996	0.072	6.870	0.212	0.0293
4170	1.328	0.093	11.368	0.557	0.0599
5210	1.66	0.113	16.800	0.748	0.0661
6250	1.992	0.133	23.116	0.982	0.0740
7300	2.324	0.152	30.266	0.985	0.0648

Figure 35 is a plot of the experimental results given in Table 13. The dimensionless deposition velocity (V+) is seen to increase rapidly with increasing particle relaxation time (τ+) to around 4. Then V+ shows a slight decrease and then a large increase reaching a peak of approximately 0.075 at a τ+ value of approximately 25. After that, V+ shows a decreasing trend at higher τ+. Although the decrease shape is unexpected, the increasing trend is similar with the toner particle dimensionless graph, and the maximum dimensionless deposition velocity is larger than the intermediate-sized particles (which approaches 0.05). This graph shows a large scale in relaxation time.

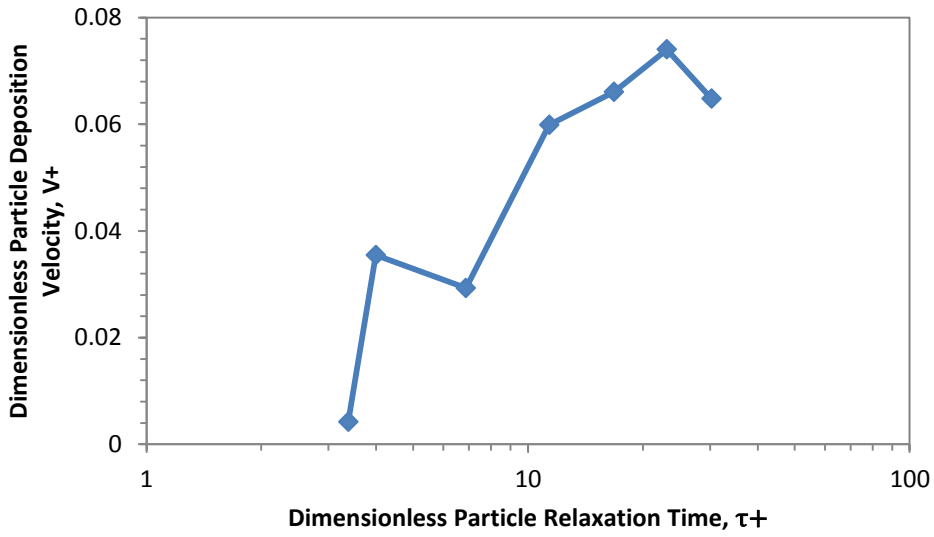

Figure 35 Experimental relationship of large particles between the dimensionless particle deposition velocity, V+ , and the dimensionless particle relaxation time, τ+

5.7 Different Particles Experimental Results Comparison

Figure 36 represents the effect of different particle deposition velocities. Beyond the Reynolds number <3000, nano particles have the largest deposition velocity among toner particles, nano and large aluminum oxide particles. With the Reynolds number increased to 8000,

the deposition velocity of all particles increases, which means particle deposition velocity will increase with enhanced turbulence. Large aluminum oxide particles show the largest deposition velocity, toner is in middle, and the smallest is nano alumina oxide particles. It can be concluded that with the diameter increased, more particles will deposit.

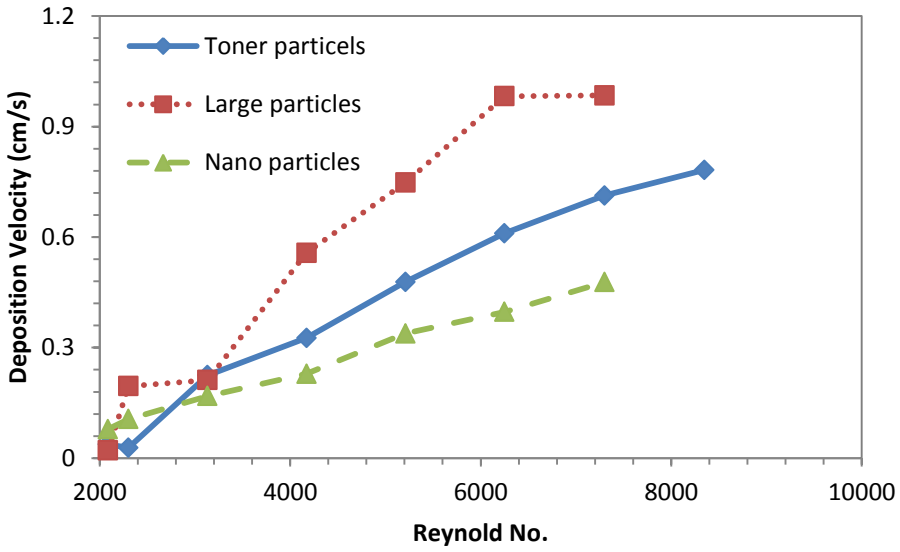

Figure 36 Effect of different particles at deposition velocity vs. Reynolds number

6 SUMMARY

Effects of turbulence and particle diameter on deposition mechanisms were theoretically and experimentally investigated. Based on the transport theory, we derive an ash deposition eddy impaction model which shows eddy impaction efficiency increases with an increase in the dimensionless eddy impaction stocks number. Different type of particles were used and collected under different rate flow conditions. Replicated experiments provided a statistical basis for analysis and indicate the validity of assuming the stable system. Comparison of the measured and calculated deposition rates provide clear evidence of the mechanisms.

6.1 Comparison

Several of the existing theories on turbulent deposition are based on the so-called "diffusion free-flight" model. In this model, particles are assumed to be transported by turbulent diffusion from the turbulent core through the boundary layer to within one "stopping distance" from the wall, at which point the particles make a "free flight" to the wall.

In the theories of Friedlander and Johnstone (Friedlander 1957), Davies (Davies 1966) and Beal (Beal 1974), particle diffusivity in the boundary layer is assumed to be the eddy momentum diffusivity of the fluid. In Davies's theory (Davies 1966), the initial free-flight velocity of the particle is assumed to be the root-mean-square fluctuating velocity of the fluid as the free flight begins. Liu and Agarwal (Liu 1974) (see Figure 37) have reported some other experiments for deposition on the walls of a vertical pipe. They also compared their experimental data with other theories (Figure 37). The theory of Liu and Ilori (Liu 1973) shows equally good

agreement with experimental data between $\tau_+ = 2$ and 20. The deposition velocities estimated by Davies' model are considerably lower in the $\tau_+ < 30$ region. Sehmel (Sehmel 1973) measured the variation in particle deposition velocity with size for particle diameters over the range estimated between 10^{-4} and 10^{2} μm. His experimental data for large particles gave deposition rates for the floor and ceiling of a wind tunnel, providing an evaluation of the influence of gravity on the effective deposition velocity (Liu 1974).

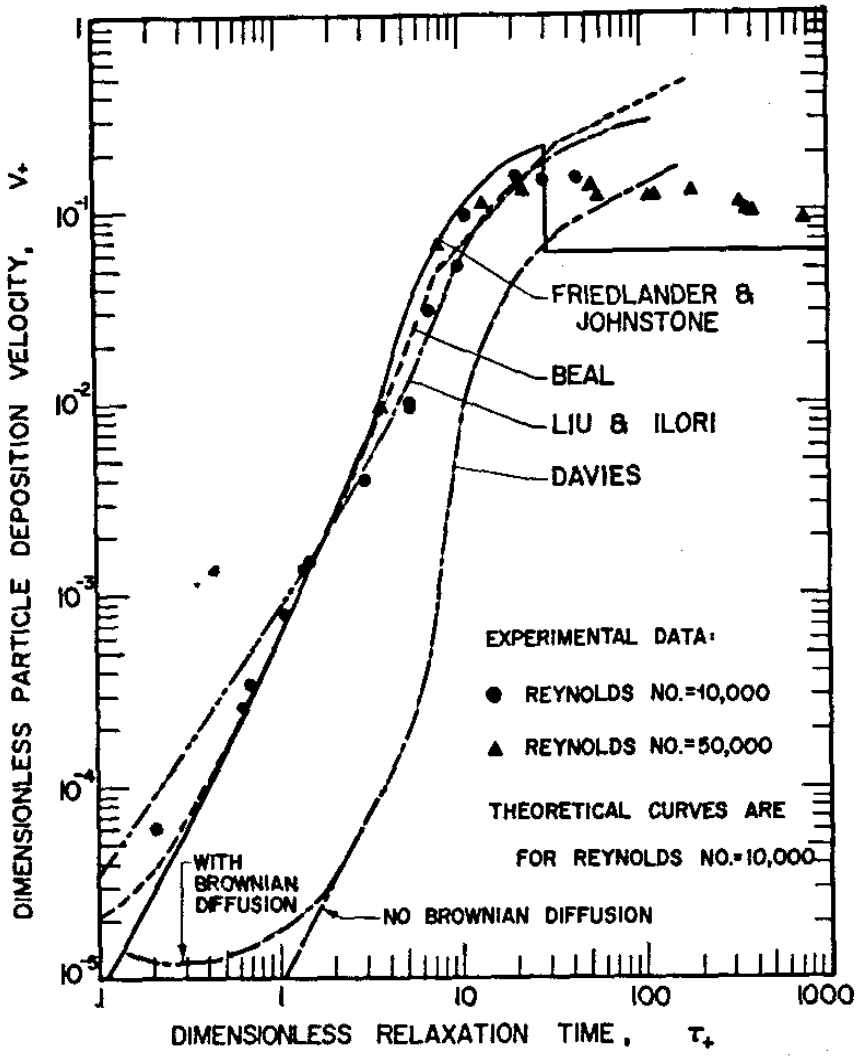

Figure 37 Comparison of theories and experiments by Benjamin Y.H. Liu and Jugal K.Agarwal

Figure 38 shows the different sized particles' deposition behavior in different relaxation times. All the particles show that the dimensionless deposition velocity increased as the dimensionless relaxation time increased. Compared with Figure 37, this trend follows the other theories' results and the experimental results show a smaller scale of the relaxation time from 0.000001 to 100. It indicates the experimental results have a good agreement with existing theories and can extend their model.

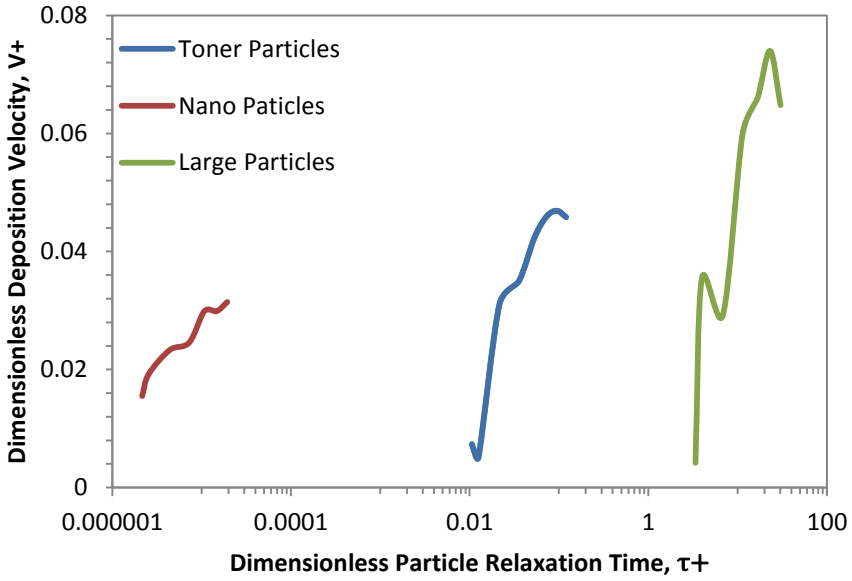

Figure 38 Different particles experimental relationship between dimensionless particle deposition velocity, V+ and dimensionless particle relaxation time, τ +

To better verify the eddy impaction model, the dimensionless Reynolds deposition velocity and particle Reynolds number is used.

Dimensionless particle deposition velocity is calculated as,

$$V(Re) = \frac{V \times d_p}{\nu} \tag{45}$$

where V is particle deposition velocity, d_p is particle diameter, and ν is the gas kinematic viscosity.

Dimensionless Reynolds number times the Stokes number is calculated as,

$$Re(Stk) = Re \times Stk = \frac{\rho \times d_{pipe} \times u_g}{\mu_g} \times \frac{\sqrt{2} u_g}{\beta \delta}$$

$$= \frac{\rho \times d_{pipe} \times u_g}{\mu_g} \times \frac{\sqrt{2} u_g}{\frac{18 u_g}{C_C \times \rho \times d_p^2} \times \frac{d_{pipe}}{2}} = \frac{\sqrt{2} C_C}{9} \frac{\rho^2 d_p^2 u_g^2}{\mu_g^2} \tag{46}$$

$$= \frac{\sqrt{2} C_C}{9} Re_p^2$$

Since we derive the dimensionless Reynolds number with Stokes number to square the particle Reynolds number, then we defined the Re(Stk)' as following:

$$Re(Stk)' = \sqrt{Re(Stk)} = \frac{\sqrt[4]{2}\sqrt{C_C}}{3} Re_p \tag{47}$$

Figure 39 shows the data plotted in these terms and indicates that particle deposition velocity increases with increasing particle Reynolds number. This dimensionless plot further agrees with the eddy impaction model that deposition velocity increases with increasing particle diameter or Reynolds number.

To compare with the eddy impaction model, the experimental eddy impaction efficiency will be,

$$\eta = \frac{V \times \frac{\dot{m}}{Volume\ \ flow}}{\frac{\dot{m}}{\pi \times \frac{d_{pipe}^2}{4}}} = \frac{V \times \pi \times d_{pipe}^2}{4 \times Volume\ flow} \tag{48}$$

where V is particle deposition velocity, d_{pipe} is diameter of the deposition pipe, $\dot{m}$ is mass flow rate, and Volume flow is gas volumetric flow rate.

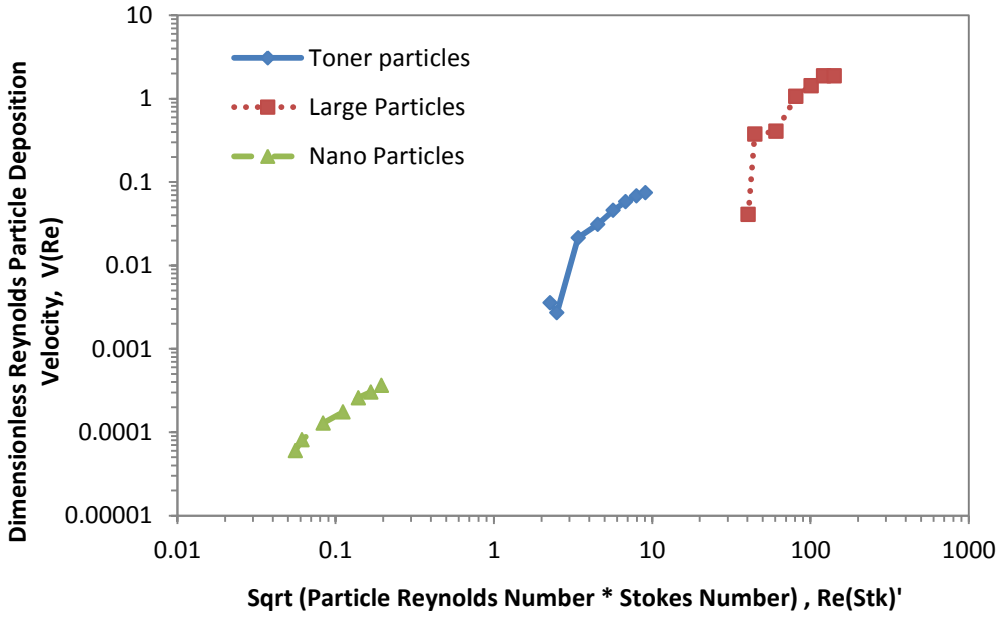

Figure 39 Different particles experimental relationships between dimensionless of Reynolds particle deposition velocity, V(Re) and sqrt (Particle Re * Stokes Number), Re(Stk)'

Figure 40 is experimental eddy impaction efficiency comparison with eddy impaction model. The different size particles shows similar increasing trend with expecting model. All three sizes particles have a limitation eddy impaction efficiency, the limitation eddy impaction efficiency for nano paticles, toner particles and large particles are 0.2, 0.3 and 0.5, separately. The highest eddy impaction efficiency is approaching 0.5, which means the maximum 50% particles will deposite. This figure shows that the experimental data correspond with the eddy impaction model, however, the further correlation need be considered to verify the model.

The predicted deposition velocity compares with the experimental deposition velocity (Figure 41) reasonably for intermediate-sized particles. However, large particle predicted

velocity exceeds the experimental data significantly, perhaps because the large particle diameter

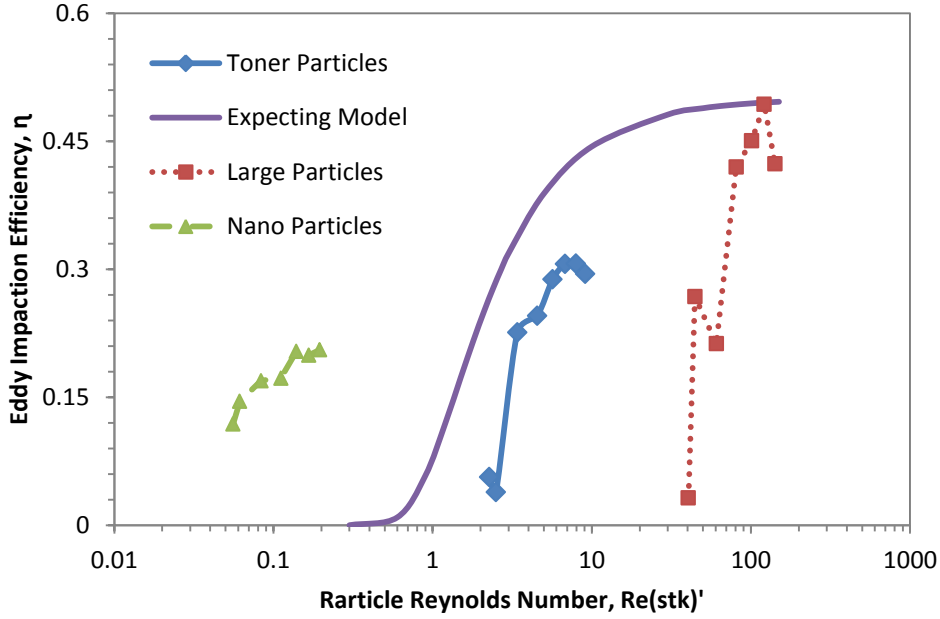

Figure 40 Comparison of experimental eddy impaction efficiency with eddy impaction model

exceeds the sublayer thickness substantially. Under such conditions, many otherwise deposited particles probably re-entrain in the bulk gas flow. The observed small particle deposition rate exceeds that of the model. The smallest particles follow the gas exactly, and no gas eddy transits the laminar sublayer, thus the predicted deposition rate is essentially zero (which is not included in the figure). However, Brownian motion also affects the small particle trajectories, which is not included in the model above. Finally, the model dependence on the ratio of particle size to boundary layer thickness was not included in these predictions.

Clearly, the current model has limitations. However, it captures the overall trends and at least much of the physics involved in this deposition mechanism and may provide a basis on which more sophisticated models can be developed.

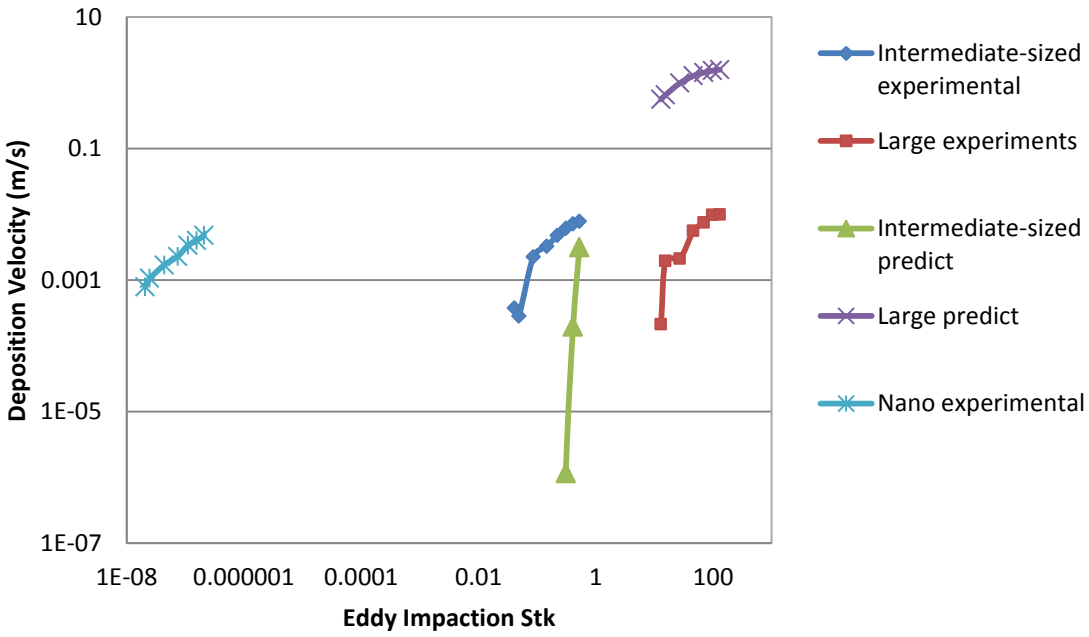

Figure 41 Different size particles predict deposition velocity vs. experimental deposition velocity

6.2 Reliability of Results

Compared with literature data, experimental deposition data reported here were high because of the experimental system. These possibilities will now be discussed. The first argument might be that roughness was present to a greater extent than in a smooth pipe. The pressure drop along the pipe dp/dl was measured; dp/dl was linear and approximately equivalent to Davis (Davies 1966) frication factor-Reynolds Number correlation for smooth pipes.

Another possible source of error was the horizontal pipe. However, the deposition flux was measured on the total inside surface of the pipe-a procedure which would cancel any gravity effects. Pipe joints were present near the area where deposition was measured. Seimel (Seimel 1966) reported that these joints can influence deposition. However, he did not observe an increased deposition characterized by factors more than 1-2 folds greater when two different pipes were together. Pipe sections used here were cut from the same pipe, and they were aligned

very carefully before each run. Further information was obtained relative to this potential problem by observing the glass covered plug used for microscopic particle count to determine the deposition flux. Vibration of the gas flow will be considered. The elimination of vibration effects was confirmed by performing deposition measurements at two different locations along the pipe.

6.3 Conclusions

The major conclusions that can be drawn from this study are as follows:

1) The method of introducing particles will affect ash deposition behavior. The experiment results show that the maximum difference at duplicate runs with blender is about 3% in average, which is much lower compared with the system without nebulizer (around 12%). It implies that the system with nebulizer is stable and only small variations in laminar and turbulent region. A nebulizer can largely improve the stability of the system and enhance the reproducibility of the experiments.

2) SF_6 can make large turbulent flows because of its density.

3) Reynolds number increased, showing the gas turbulence improved, and it's easily understood that ash particles tend to deposit more with the turbulence increased. This agrees with intuition.

4) Through those reproducibility experiments, we find that with the turbulence enhanced the particles prefer to deposit in further sections, which also agrees with intuition.

5) In the transition region, the deposition velocity distribution is a little random, however, it still follows conclusion 3) and conclusion 4) particles prefer to deposit more in further sections.

6) The different sized particles experiments confirm the eddy impaction model that the deposition velocity will increase with the particle diameter increased.

The experimental results prove the eddy impaction model, so we can conclude: The eddy impaction efficiency increases with increasing particle/gas turbulent intensity (Reynolds number) and decreases with increasing boundary layer thickness. Eddy impaction efficiency increases with increasing particle size for a given gas velocity fluctuating environment.

6.4 Recommendations

Recommendations for future research on the effect of eddy impaction on ash deposition include:

1) More different size particles should be used. This can provide more size information to verify the size affection on eddy impaction.
2) Similar experiments should be performed for larger Reynolds number which means more intense turbulence. This would expand particles' deposit behaviors.
3) More analysis should focus on the transition region. The more random data needs be further investigated to explore the deposition mechanism.
4) Experimental system may need to be improved to enhance the precision of the experimental data.
5) Further correlation should be considered to verify the eddy impaction model and finally apply the model to reality.

7 REFERENCE

Bakker, R. R., Jenkins, B.M. and Williams, R.B. (2002) Fluidized Bed Combustion of Leached Rice Straw. *Energy and Fuels,* 16**,** 356-365.

Baxter, L. L. (1993) Ash Deposition during Biomass and Coal Combustion: A Mechanistic Approach. *Biomass and Bioenergy,* 4**,** 85-102.

Baxter, L. L. (1996) Influence of ash deposit chemistry and structure on physical and transport properties. *Abstracts of Papers of the American Chemical Society,* 211**,** 112-FUEL.

Baxter, L. L. (1998a) Influence of ash deposit chemistry and structure on physical and transport properties. *Fuel Processing Technology,* 56**,** 81-88.

Baxter, L. L. 2000. Ash Deposit Formation and Deposit Properties: A Comprehensive Summary of Research Conducted at Sandia's Combustion Research Facility - Final Report. 92-118. Livermore: Sandia National Laboratory, CA.

Baxter, L. L., Fletcher, T.H., Ottesen, D.K. (1988) Spectral Emittance Measurements of Coal Particles. *Energy and Fuels,* 2**,** 423-430.

Baxter, L. L., Lind, T., Kauppinen, E., and Robinson, A. 2001. Thermal properties of recovery boiler deposits. In *International Chemical Recovery Conference, Jun 11-14 2001,* 133-138. Whistler, BC: Technical Assoc. of the Pulp and Paper Industry Press.

Baxter, L. L., Miles, T.R., Miles(Jr.), T.R., Jenkins, B.M., Milne, T., Dayton, D., Bryers, R.W., and Oden, L.L. (1998b) The behavior of inorganic material in biomass-fired power boilers: field and laboratory experiences. *Fuel Processing Technology,* 54**,** 47-78.

Beal, S. K. (1974) Deposition of Particles in Turbulent Flow on Channel or Pipe Walls. *Nucl.Sci. Engng,* 40.

Beer, J. M., Sarofim, A. F., Barta, L. E. 1992. Inorganic Transformations and Ash Deposition During Combustion. In: Benson S.A.: New York: Engineering Foundation.

Benson, S. A., Jones, M. L., Harb, J. N.,. 1993. Fundamentals of Coal Combustion. In:Smoot L.D: New York: Elesvier Science.

Boow, J. a. P. R. G. (1969) Fireside Deposits and Their Effect on Heat Transfer in a Pulverized-fuel-fired Boiler: Part III. The Influence of the Physical Characteristics of the Deposit on Its Radiant Emittance and Effective Thermal Conductance. *Journal of the Institute of Fuel,* 42**,** 412-419.

Coda, B., Aho M., Berger R. and Hein, K.R.G (2001) Behavior of Chlorine and Enrichment of Risky Elements in Bubbling Fluidized Bed Combustion of Biomass and Waste Assisted by Additives. *Energy and Fuels,* 15**,** 680-690.

Davies, C. N. 1966. *Deposition from Moving Aerosols*. New York: In Aerosol Science Academic Press.

denToonder, J. M. J. & F. T. M. Nieuwstadt (1997) Reynolds number effects in a turbulent pipe flow for low to moderate Re. *Physics of Fluids,* 9**,** 3398-3409.

Frank, M. W. 2003. *Fluid Mechanics, Fifth edition*. McGraw-Hill Higher Education.

Friedlander, S. K. a. J., H. F (1957) Deposition of Suspended Particles from Turbulent Gas Streams. *Ind. Engeg Chem,* 49**,** 1151.

Green, J. H. (1994) TRENDS AND OUTLOOK FOR BIOMASS ENERGY. *Energy Engineering,* 91**,** 18-28.

Hein, K. R. G. & J. M. Bemtgen (1998) EU clean coal technology - co-combustion of coal and biomass. *Fuel Processing Technology,* 54**,** 159-169.

Hurley, J. P., Nowok, J. W., Strobel, T. M., O' Keefe, C. A., Bieber, J. A. and Dockter, B. A. (1996) Rates and Mechanisms of Strength Development in Low Temperature Ash Deposits. *Applications of Advanced Technology to Ash-Related Problems in Boilers,* 83-95.

Hutagalung, M. 2008. Understanding Coal Analysis. In *Majare Magazine*.

Jagota, A., P. R. Dawson & J. T. Jenkins (1988) AN ANISOTROPIC CONTINUUM MODEL FOR THE SINTERING AND COMPACTION OF POWDER PACKINGS. *Mechanics of Materials,* 7**,** 255-269.

Jagota, A. a. C. Y. H. (1990) The Effective Thermal Conductivity of a Packing of Spheres. *Transactions of the ASME, Journal of Applied Mechanics,* 57**,** 789-791.

Jenkins, B. M., Miles, T.R. Jr, Baxter, L.L. and Miles, T.R. (1998a) Combustion properties of Biomass. *Fuel Processing Technology,* 54.

Jenkins, B. M., Miles, T.R. Jr, Baxter, L.L. and Miles, T.R. (1998b) Combustion properties of Biomass. *Fuel Processing Technology,* 54**,** 17-46.

Joller, M., T. Brunner & I. Obernberger (2007) Modeling of aerosol formation during biomass combustion for various furnace and boiler types. *Fuel Processing Technology,* 88**,** 1136-1147.

Kalmanoitch, D. P., and M. Frank. 1988. An Effective Model of Viscosity for Ash Deposition Phenomena. In *Mineral Matter and Ash Deposition from Coal*. Santa Barbra, CA.

Kaufmann, H., Nussbaumer, Th., Baxter, L. and Yang, N. (2000) Deposit formation on a single cylinder during combustion of herbaceous biomass. *Fuel Processing Technology,* 79**,** 141-151.

Kweon, S. C., E. Ramer & A. L. Robinson (2003) Measurement and simulation of ash deposit microstructure. *Energy & Fuels,* 17**,** 1311-1323.

Lee, F. C. C., and Lockwood, F. C (1999) Modeling Ash Deposition in Pulverized Coal-fired Applications. *Progress in Energy and Combustion Science,* 25**,** 117-132.

Liu, B. Y. H. a. A., J. K. (1974) Experimental Observation of Aerosol Deposition in Turbulent Flow. *Journal of Aerosol Science,* 5**,** 145.

Liu, B. Y. H. a. I., T. A. 1973. Inertial Deposition of Aerosol Particles in Turbulent Pipe Flow. In *Presented at the ASME Symposium on Flow Studies in Air and Water Pollution*, 20-22. Altanta, Georgia.

Lokare, S. S. 2003. Investigation of Ash Deposition and Corrosion Mechanisms in Combustion of Bio-fuels and Fuel Blends in a Pilot-Scale Facility. In *Chemical Engineering*. Provo: Brigham Young University.

Lokare, S. S. 2008. Mechanistic investigation of ash deposition in pulverized-coal and biomass combustion. In *Chemical Engineering*. Provo: Brigham Young University.

Mann, M. K., Span, Pamela L. 1999. The Net CO_2 Emissions and Energy Balances of Biomass and Coal-Fired Power Systems. National Renewable Energy Laboratory.

Postelnicu, A. (2007) Effects of thermophoresis particle deposition in free convection boundary layer from a horizontal flat plate embedded in a porous medium. *International Journal of Heat and Mass Transfer,* 50**,** 2981-2985.

Raask, E. (1984) CREATION, CAPTURE AND COALESCENCE OF MINERAL SPECIES IN COAL FLAMES. *Journal of the Institute of Energy,* 57**,** 231-239.

Robinson, A., Buckley, S.G. and Baxter, L.L. (2001a) Experimental Measurements of the Thermal Conductivity of Ash Deposit: Part 1. Measurement Technique. *Energy and Fuels,* 15**,** 66-74.

Robinson, A., Buckley, S.G., Yang, N. and Baxter, L.L. (2001b) Experimental measurements of the Thermal Conductivity of ash deposits: Part 2. Effects of Sintering and Deposit Microstructure. *Energy and Fuels,* 15**,** 75-84.

Robinson, A., Junker, H., Buckley, S.G., Sclippa, G. and Baxter, L.L. (1998) Interaction between coal and biomass when cofiring. *Twenty-Seventh Symposium (International) on Combustion/The Combustion Institute***,** 1351-1359.

Rosner, D. E. 1986. *Transport Processes in Chemically Reacting Flow Systems*.

Schlichting, H. 1968. *Boundary Layer Theory*. New York: McGraw-Hill.

Sehmel, G. A. (1973) Particle Eddy Diffusivities and Deposition Velocities for Isothermal Flow and Smooth Surfaces. *Journal of Aerosol Science,* 4**,** 145.

Seimel , G. A. 1966. Richland, Washington: Battelle Memorial Institute publication.

Srinivasachar, S., Helble, J. J., and Boni, A. A. (1990a) Mineral Behavior During Coal Combustion in Pyrite Transformations. *Symposium on Ash Deposition, Progress in Energy and Combustion Science,* 16**,** 281-92.

Srinivasachar, S., Helble, J.J., and Boni, A.A. (1990b) Mineral behavior during coal combustion. 1. Pyrite transformations. *Symposium on Ash Deposition, Apr 1989 Progress in Energy and Combustion Science,* 16**,** 281-292.

Urbain, G. (1981) Viscosity of Silica Melts. *Journal of the British Ceramic Society* 80.

Vuthaluru, H. B. (2004) Investigations into the pyrolytic behaviour of coal/biomass blends using thermogravimetric analysis. *Bioresource Technology,* 92**,** 187-195.

Wall T.F., B. S. P., Baxter L.L., Young B.C. and Grisanti A.A. 1996. Ash deposit properties and radiative transfer in coal fired plant - Current understanding and new developments. In *Applications of Advanced Technology to Ash-Related Problems in Boilers,* ed. L. B. a. R. DeSollar, 67-82. Plenum Press, New York.

Wall, T. F. 1992. Mineral matter transformations and ash deposition in pulverized coal combustion. In *Proceedings of the 24th International Symposium On Combustion, Jul 5-10 1992*, 1119-1126. Sydney, Engl: Publ by Combustion Inst, Pittsburgh, PA, USA.

Wall, T. F., Bhattacharya, S.P., Baxter, L.L., Richards, G. and Harb, J.N. (1995) The character of ash deposits and the thermal performance of furnaces. *Fuel Processing Technology,* 44**,** 143-153.

Wall, T. F., Bhattacharya, S.P., Zhang, D.K., Gupta, R.P., and He, X. (1993) Properties and thermal effects of ash deposits in coal-fired furnaces. *Progress in Energy and Combustion Science,* 19**,** 487-504.

Walsh, P. M., Sayre, A. N., Loehden, D. O., Monroe, L. S., Beer, J. M, Sarofim, A. F. (1990). *Progress in Energy and Combustion Science,* 16.

Yuanyuan Shao, C. X., Jesse Zhu, Fernando Preto, Jinsheng Wang, Guy Tourigny, Chadi Badour, and Hanning Li (2010) Ash Deposition during Co-firing Biomass and Coal in a Fluidized-Bed Combustor. *Energy Fuels,* 24**,** 4681-4688.

Zbogar, A., F. J. Frandsen, P. A. Jensen & P. Glarborg (2005) Heat transfer in ash deposits: A modelling tool-box. *Progress in Energy and Combustion Science,* 31**,** 371-421.

Zbogar, A., Frandsen, F. J, Jensen, P. A and Glarborg, P (2006) Heat Transfer in Ash Deposits: A Modelling Tool-box. *Progress in Energy and Combustion Science,* 31**,** 371-421.

Zygarlicke, C. J. & E. N. Steadman (1990) ADVANCED SEM TECHNIQUES TO CHARACTERIZE COAL MINERALS. *Scanning Microscopy,* 4**,** 579-590.